Aerospace Science and Technology 126 (2022) 107587

Contents lists available at ScienceDirect

Aerospace Science and Technology

www.elsevier.com/locate/aescte

Theoretical and numerical analysis of effects of sudden expansion and contraction on compressible flow phenomena in Hyperloop system

Jihoon Kim [a], Thi Thanh Giang Le [b], Minki Cho [c], Jaiyoung Ryu [a,b,*]

[a] Department of Mechanical Engineering, Chung-Ang University, Seoul 06974, Republic of Korea
[b] Department of Intelligent Energy and Industry, Chung-Ang University, Seoul 06974, Republic of Korea
[c] Hyper Tube Express (HTX) Research Team, Korea Railroad Research Institute, Gyeonggi-do 16105, Republic of Korea

ARTICLE INFO

Article history:
Received 19 January 2022
Received in revised form 15 March 2022
Accepted 22 April 2022
Available online 29 April 2022
Communicated by Mehdi Ghoreyshi

Keywords:
Hyperloop system
Compressible flow
Aerodynamics
Shock wave
Sudden expansion and contraction

ABSTRACT

With rapid changes in lifestyle patterns and recent technological advancements, there is an increasing demand for efficient, convenient, and eco-friendly transportation systems. The Hyperloop system, which is a tube–train system, was introduced with the aim of catering to the demand for improved transportation facilities. The primary factors of the Hyperloop system such as the point of departure (pod), standstill, and transfer are directly dependent on the change in the cross-sectional area of the tube such as stations. In this study, the effects of sudden expansion and contraction were analyzed though numerical simulations with respect to the blockage ratio (BR), expansion ratio (ER), and contraction ratios (CR). Furthermore, the propagation Mach number and magnitude of pressure waves were predicted through theoretical consideration. Under sudden expansion and contraction of tube, the first leading shock wave (LSW_1), reflected expansion wave (REW), second leading shock wave (LSW_2), reflected shock wave (RSW), and third leading shock wave (LSW_3) are generated in this system. The propagation Mach number and pressure magnitude of LSW_1 increase with an increase in the BR. The Mach number of REW decreases with an increase in the BR. The propagation Mach number of LSW_2 increases with the BR and with a decrease in the ER owing to the pressure behind the shock wave. The propagation Mach number of RSW decreases with an increase in the BR and with a decrease in the CR, and that of LSW_3 increases with an increase in the BR and with a decrease in the CR. The drag coefficient decreases when REW reaches the pod because the expansion wave decreases the pressure of flow field. Owing to the similar minimum drag coefficient, the difference of drag coefficient increases with an increase in the BR. In this study, the predicted Mach number and pressure magnitude under quasi-one-dimensional assumption are in good agreement with the simulation results. Therefore, this study can aid the design of expanded and contracted zones considering the formation of the shock wave.

1. Introduction

Recent technological advances have resulted in strong market competition across the world, resulting in an increase in the demand for innovative and advanced technologies. The evolving lifestyle patterns have given the platform for several industry verticals, and transportation is among the fastest growing sectors across the world. The subsequent demand for faster domestic cars, high-speed trains, and airplanes has given rise to numerous innovations in recent years. Recent advances in high-speed transportation have pivoted the evolution of this field. Oster introduced an evacuated tube transport, which is a train that travels in a vacuum tube [1]. This evacuated tube transport has numerous advantages including high-speed, low aerodynamic forces, efficient operation, and low cost. As a developed evacuated tube transport, the Hyperloop system has attracted the most attention among the list of vacuum-tube transport systems across the world. The Hyperloop system, which was introduced by Elon Musk in 2013 [2], is based on a concept wherein a pressurized capsule (i.e., a pod) travels in a sub-vacuum tube (i.e., 1/1000 atm) with a target speed nearing the speed of sound (i.e., 1250 km/h). There has been a

* Corresponding author at: Department of Mechanical Engineering and Department of Intelligent Energy and Industry, Chung-Ang University, Seoul 06974, Republic of Korea.
E-mail addresses: kimjihoon95@cau.ac.kr (J. Kim), giangletthanh95@cau.ac.kr (T.T.G. Le), mkcho@krri.re.kr (M. Cho), jairyu@cau.ac.kr (J. Ryu).

https://doi.org/10.1016/j.ast.2022.107587

Nomenclature

A_{CT}	Cross-sectional area of contraction tube
A_{EZ}	Cross-sectional area of expanded zone
A_P	Cross-sectional area of pod
A_{PT}	Cross-sectional area of primary tube
BR	Blockage ratio (A_P/A_{PT})
C_d	Drag coefficient
CR	Contraction ratio (A_{ET}/A_{CT})
d_{CT}	Diameter of contraction tube
d_{EZ}	Diameter of expanded zone
d_h	Hydraulic diameter
d_{PT}	Diameter of primary tube
ER	Expansion ratio (A_{ET}/A_{PT})
F_d	Drag force
l_{EZ}	Length of expanded zone
LSW_1	First leading shock wave
LSW_2	Second leading shock wave
LSW_3	Third leading shock wave
$\dot{m}$	Mass flow rate
M	Mach number
M_{LSW_1}	Mach number of first leading shock wave
M_{LSW_2}	Mach number of second leading shock wave
M_{LSW_3}	Mach number of third leading shock wave
M_p	Mach number of pod
M_{REW}	Mach number of reflected expansion wave
M_{RSW}	Mach number of reflected shock wave
p	Static pressure
p_o	Stagnation pressure
p_{o,LSW_1}	Stagnation pressure behind LSW_1
p_{o,LSW_3}	Stagnation pressure behind LSW_3
$p_{o,RSW}$	Stagnation pressure behind RSW
p_∞	Base pressure (101.325 Pa)
R	Individual gas constant
Re	Reynolds number
REW	Reflected expansion wave
RSW	Reflected shock wave
T	Static temperature
T_o	Stagnation temperature
T_{o,LSW_1}	Stagnation temperature behind LSW_1
T_∞	Base temperature (300 K)
v	Velocity
v_p	Velocity of pod
γ	Specific heat ratio
ρ	Density
μ	Viscosity

Superscript

s	Shock-fixed coordinates system
p	Pod-fixed coordinates system

Subscript

a	Local quantity in front of shock wave
b	Local quantity behind shock wave

considerable amount of research related to this system, most of it being focused on factors such as the pressure of tube, speed of pod, and structure.

The parametric study was conducted for varying the speed of pod [3–8]; tube pressure [3–6]; blockage ratio (BR) (i.e., a cross-sectional area ratio of pod-to-tube) [3,5–8]; pod shape [4,8]; temperature [3,9]; and pod length [3]. The aerodynamic drag significantly increases with the speed of pod, tube pressure, and BR owing to the high-pressure field in front of the pod. Furthermore, the aerodynamic drag slightly increases with an increase in pod length at low-temperature. Previous studies reported the oblique shock wave that is formed behind the tail of pod, and the oblique shock wave significantly increases the aerodynamic drag. However, the compressible flow behavior such as the propagation of wave cannot be considered because these studies [3–9] conducted steady-state simulations. The aerodynamic drag and the oblique shock wave were also analyzed with unsteady-state simulations for various speeds of the pod [10–12]; tube pressure [10,11]; and BR [10,11,13]. Although the tendencies were similar in the steady-state simulations, the propagation of pressure waves was observed in the aforementioned studies.

When an object moves at a high speed in a confined space, various pressure waves are generated, and the compressible flow phenomena is more apparent than in open spaces owing to the choked flow. The compressible flow phenomena on a high-speed projectile in a tube were comprehensively analyzed with regard to theory, experiment, and simulation [14]. The compression and expansion waves are generated in the tube, and these waves propagate in opposite directions. Furthermore, oblique shock and trailing shock waves are generated behind the projectile after it reaches a critical speed. They concluded that the pressure waves severely change the flow fields inside a tube, and the aerodynamic characteristics vary owing to the pressure waves. Jang et al. [15] analyzed the compressible flow phenomena and aerodynamic characteristics for varying speeds of the pod in the Hyperloop system through numerical simulation and theoretical consideration. They observed that the leading shock wave (LSW) and expansion wave are generated at a pod speed of 100 to 300 m/s. When the pod reaches a critical speed (i.e., occurrence of choking phenomenon), the oblique shock and trailing shock waves are generated. They concluded that the flow regimes can be divided through the compressible flow phenomena such as choking and oblique shock wave. Sui et al. [16] analyzed the aerothermodynamic behavior under choked flow in the Hyperloop system. They performed numerical simulations, and focused on the oblique shock wave for various BR, concluding that the presence of choked flow results in an increase in the pressure, temperature in front of pod, and the aerodynamic drag.

In the Hyperloop system, the change in cross-sectional area (i.e., sudden expansion and contraction) of the tube, such as in stations, should be considered for the departure, standstill, and transfer [17,18]. Because the LSW with high-pressure propagates to the expanded zone, the compressible flow behaviors that vary according to the change in the cross-sectional area are important in operations for the Hyperloop system. Furthermore, the pressure wave is transmitted and reflected at the location where the cross-sectional area changes, affecting the aerodynamic characteristics of the Hyperloop system. Trengrouse and Soliman [19] theoretically analyzed the effects of sudden changes in flow area on pressure waves. They predicted the amplitudes of the reflected and transmitted waves at abrupt changes in flow area, and concluded that the predicted amplitudes were in good agreement with experimental results under the isentropic assumption. Hall and Orme [20] investigated the compressible flow through a sudden enlargement in a pipe with theoretical and experimental considerations. They concluded that the Mach numbers in the entrance to enlargement as well as in the downstream are accurately predicted within the specific range of area ratio.

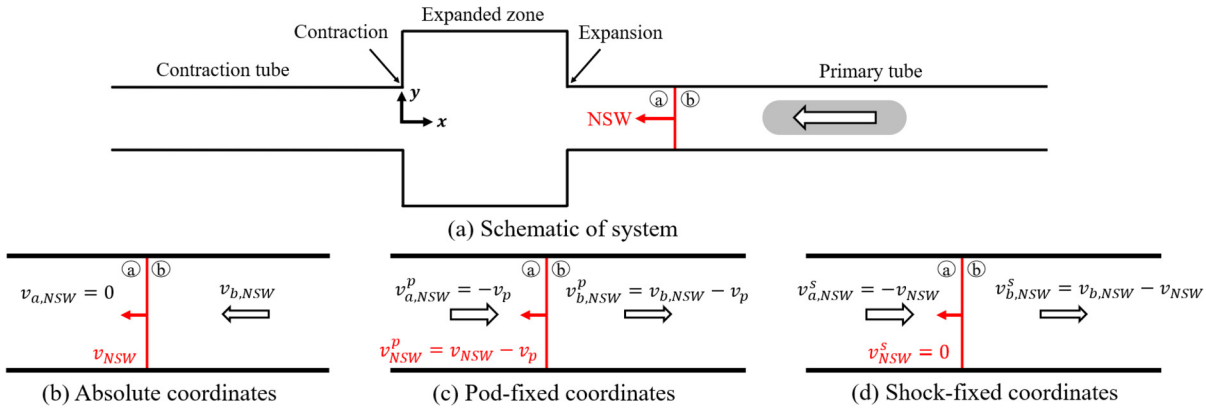

Fig. 1. Normal shock wave (NSW) for each coordinate system; (a) Absolute coordinates, (b) Pod-fixed coordinates, and (c) Shock-fixed coordinates. Here, subscript a and b indicate local quantities in front of and behind normal shock wave. Superscripts p and s indicate pod-fixed and shock-fixed coordinates systems, respectively.

Although these studies were significant, the effects of sudden expansion and contraction of a tube in the Hyperloop system on the compressible flow phenomena and aerodynamic characteristics have not been studied. Our study theoretically and numerically analyzed the compressible flow phenomena and aerodynamic characteristics considering the sudden expansion and contraction of the tube for varying BRs at a transonic speed of pod (i.e., $M = 0.864$). More specifically, the propagation speed and magnitude of pressure waves were predicted through a theoretical consideration under isentropic and quasi-1D flow assumption, and were compared with the simulation results.

2. Theoretical consideration

2.1. Assumptions and normal shock relations

Based on the theoretical consideration, the magnitude and propagation speed of pressure waves, such as normal shock wave and expansion wave, were predicted through several assumptions for ideal gas, quasi-1D, and isentropic flow. In the Hyperloop system, the high-pressure field and low-pressure field are formed by the movement of pod because the air is compressed in front of the nose of the pod, which generates the compression wave, and because the air is expanded on the curved surface of the tail of the pod, which makes the expansion wave. In an open space, the compression wave propagates in all directions when an object moves at subsonic speed. Thus, the compression wave dissipates owing to the energy loss. In contrast, the compression wave propagates along the axial direction of the tube with low dissipation because it is restricted by the wall of tube. The compression wave is repeatedly generated when an object moves from the subsonic to supersonic speed. Furthermore, the compression waves possess a gradual pressure profile, thus resulting in a difference in local speed of sound at each point. The speed of sound increases with an increase in temperature, and as a result, the compression wave becomes an intense wave as it propagates. Therefore, the compression waves generated by the movement of pod propagate with low dissipation, and develop into a normal shock wave because a compression wave is faster than an anterior compression wave [21–23].

The absolute, pod-fixed, and shock-fixed coordinates systems are considered in the theoretical consideration to quantitatively analyze the normal shock wave and expansion wave in this study. In the absolute coordinates system, an observer is located outside the system. In the pod-fixed coordinates system, the observer is located at the pod. In other words, the pod is stationary and surrounding fluid flows relative to the pod. The shock-fixed coordinates system is related to the observer located on the shock wave, and thus, the speed of shock wave is zero in this coordinates system. Fig. 1 presents the expression of velocity for various coordinates systems, and these expressions were used to derive the equations. The normal shock wave (NSW), shown in Fig. 1, represents all shock waves covered in this study, i.e., first leading shock wave (LSW_1), second leading shock wave (LSW_2), third leading shock wave (LSW_3), and reflected shock wave (RSW) in section 2.3 and Fig. 2. The local quantities such as pressure, density, temperature, and Mach number vary discontinuously across the normal shock wave. Accordingly, the local quantities are defined as the locations; subscript a and b indicates the local quantities in front of and behind the normal shock wave, and superscript s indicates the shock wave coordinates system. The normal shock relations for these quantities can be expressed in shock-fixed coordinates system as follows [21–23]:

$$\frac{p_b}{p_a} = \frac{2\gamma\left(M_a^s\right)^2 - (\gamma - 1)}{\gamma + 1}, \tag{1}$$

$$\frac{\rho_b}{\rho_a} = \frac{(\gamma + 1)\left(M_a^s\right)^2}{(\gamma - 1)\left(M_a^s\right)^2 + 2}, \tag{2}$$

$$\frac{T_b}{T_a} = \frac{\left[(\gamma - 1)\left(M_a^s\right)^2 + 2\right]\left[2\gamma\left(M_a^s\right)^2 - (\gamma - 1)\right]}{(\gamma + 1)^2\left(M_a^s\right)^2}, \tag{3}$$

$$M_b^s = \sqrt{\frac{(\gamma - 1)\left(M_a^s\right)^2 + 2}{2\gamma\left(M_a^s\right)^2 - (\gamma - 1)}}, \tag{4}$$

where

$$M_a^s = \frac{v_a^s}{\sqrt{\gamma R T_a}}, \tag{5}$$

$$M_b^s = \frac{v_b^s}{\sqrt{\gamma R T_b}}. \tag{6}$$

Here, p is the static pressure, ρ is the fluid density, T is the static temperature, v is the flow velocity, M is the Mach number, γ is the specific heat ratio, and R is the individual gas constant.

2.2. Converging–diverging nozzle relation

In the Hyperloop system, the cross-sectional area between the tube and the pod is similar to a converging–diverging (i.e., de Laval) nozzle. To analyze the flow through converging–diverging nozzle, a quasi-1D flow is assumed [24–26]. The convergent and divergent sections exist owing to the nose and tail of the pod, respectively. In the converging–diverging nozzle, flow regimes can be observed with respect to the condition of upstream and downstream pressure. When the downstream pressure is relatively high, the incoming flow of the subsonic speed accelerates to the throat, and decelerates in the divergent section such that the fluid flows at subsonic speed at the exit. If the downstream pressure is lower than that of previous condition, the choked flow may occur at the throat, and a normal shock wave is formed in the divergent section. Thus, the flow experiences a discontinuous change across the normal shock wave. In this condition, the supersonic flow is observed from the throat to normal shock wave, but this flow is not fully accelerated, mainly because of the shock wave. Under the condition when there is enough low downstream pressure, the sonic flow at the throat accelerates until the exit. Thus, the supersonic flow is observed in the divergent section (i.e., supersonic flow at the exit of nozzle). When the Hyperloop system is considered in the pod-fixed coordinates system, the flow comes toward the pod at the same speed as the pod and experiences the convergent section by passing between the tube and the pod. Furthermore, the straight section can be regarded as a throat, and the divergent section exists between the tube and tail of the pod. Therefore, the converging–diverging nozzle relation under the choking condition in the pod-fixed coordinates system is expressed as follows:

$$\frac{A_T}{A_T - A_P} = \frac{1}{M^p}\left[\frac{1 + \left(\frac{\gamma-1}{2}\right)\left(M^p\right)^2}{1 + \left(\frac{\gamma-1}{2}\right)}\right]^{\frac{\gamma+1}{2(\gamma-1)}}. \tag{7}$$

Here, A_T and A_P are the cross-sectional areas of the tube and pod, respectively. The superscript p indicates the pod-fixed coordinates system. In the converging–diverging nozzle, two solutions can be obtained from Eq. (7) under the choked flow at the throat and isentropic flow conditions; one is a critical Mach number, which represents the subsonic Mach number at the entrance to nozzle, and the other is the exit Mach number, which represents the supersonic Mach number at the exit of the nozzle.

2.3. Prediction of normal shock wave

Fig. 2 shows the pressure waves for the LSW_1, LSW_2, REW, LSW_3, and RSW. As mentioned above, LSW_1 is generated by the movement of pod, and it propagates to the expanded zone. As shown in Fig. 2(a), the Mach number behind LSW_1 under isentropic and choked flow conditions can be expressed as follows [15]:

$$M_{b,LSW_1}^p = \frac{M_{LSW_1}\left[(\gamma+1)M_p - 2M_{LSW_1}\right] + 2}{\sqrt{\left[2\gamma\left(M_{LSW_1}\right)^2 - (\gamma-1)\right]\left[(\gamma-1)\left(M_{LSW_1}\right)^2 + 2\right]}}, \tag{8}$$

where

$$M_{LSW_1} = \frac{-v_{LSW_1}}{\sqrt{\gamma R T_{a,LSW_1}}}, \tag{9}$$

$$M_p = \frac{-v_p}{\sqrt{\gamma R T_{a,LSW_1}}}. \tag{10}$$

Here, M_{b,LSW_1}^p is the Mach number behind LSW_1 in the pod-fixed coordinates system. M_{LSW_1} and M_p are the Mach number of LSW_1 and the pod in the absolute coordinates system, respectively. The quantities between LSW_1 and nose of pod were assumed to be identical under isentropic flow assumption. Accordingly, the M_{b,LSW_1}^p can be determined as the critical Mach number from Eq. (7) under choked flow condition, and M_{LSW_1} can be obtained from Eqs. (8)–(10). Accordingly, all local quantities behind LSW_1 are determined from Eqs. (1)–(6).

Once LSW_1 is transmitted to the expanded zone, LSW_2 is generated, which then propagates in the expanded zone when the flow is fully developed (as shown in Fig. 2(b)). As the flow enters to the expanded zone, that experiences the effect of converging-diverging nozzle owing to the streamline [27]. When the flow accelerates owing to the sudden expansion, the location of maximum flow velocity is near the entrance to the expanded zone. It was assumed that the flow induced by the pod was choked at the entrance to the expanded zone. To predict the quantities behind LSW_2, the mass flow rate behind LSW_2 was assumed to be identical to that at the entrance to the expanded zone. Thus, the compressible mass flow rate can be expressed as follows [21–23]:

$$\dot{m} = A\frac{p_o}{\sqrt{T_o}}\sqrt{\frac{\gamma}{R}}M\left(1 + \frac{\gamma-1}{2}M^2\right)^{-\frac{\gamma+1}{2(\gamma-1)}}. \tag{11}$$

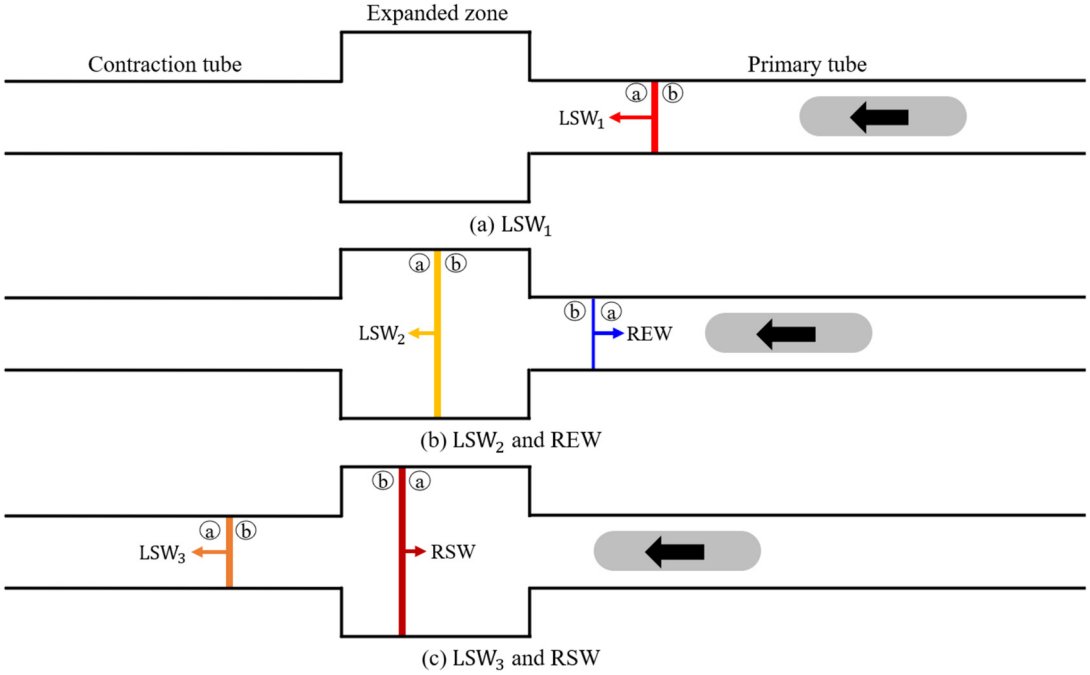

Fig. 2. Pressure waves with respect to movement of pod. First leading shock wave (LSW_1), second leading shock wave (LSW_2), reflected expansion wave (REW), third leading shock wave (LSW_3), and reflected shock wave (RSW).

Here, p_o and T_o are the stagnation pressure and temperature, respectively. When the flow is assumed to be choked, the Mach number in Eq. (11) is equal to one. Thus, the mass flow rate can be obtained from the stagnation pressure and temperature. The stagnation pressure and temperature at the entrance to the expanded zone were assumed to be identical behind LSW_1 from the isentropic flow assumption.

As mentioned above, the mass flow rate at the entrance to the expanded zone and that behind LSW_2 were assumed to be identical under isentropic flow. To predict the local quantities behind LSW_2, the equation of compressible mass flow rate was applied under the choking condition at the entrance to the expanded zone. Therefore, the Mach number behind LSW_2 can be expressed through the mass conservation between the entrance to the expanded zone and LSW_2:

$$M_{b,LSW_2} = \frac{1}{(ER)\cdot M_{LSW_2}} \frac{p_{o,LSW_1}}{p_\infty} \sqrt{\frac{T_\infty [(\gamma-1)] \left(M_{LSW_2}\right)^2 + 2}{T_{o,LSW_1}\left[2\gamma\left(M_{LSW_2}\right)^2 - (\gamma-1)\right]}} \left(\frac{\gamma+1}{2}\right)^{-\frac{\gamma+1}{2(\gamma-1)}}, \tag{12}$$

where

$$M_{LSW_2} = \frac{-v_{LSW_2}}{\sqrt{\gamma R T_{a,LSW_2}}}, \tag{13}$$

$$p_{o,LSW_1} = p_{b,LSW_1}\left[1 + \frac{\gamma-1}{2}\left(M_{b,LSW_1}\right)^2\right]^{\frac{\gamma}{\gamma-1}}, \tag{14}$$

$$T_{o,LSW_1} = T_{b,LSW_1}\left[1 + \frac{\gamma-1}{2}\left(M_{b,LSW_1}\right)^2\right]. \tag{15}$$

Here, M_{LSW_2} is the Mach number of LSW_2 in absolute coordinates system. p_∞ and T_∞ are the freestream pressure and temperature (i.e., operating pressure and temperature of the tube), respectively. The expansion ratio (ER) is defined as the cross-sectional area of expansion-to-primary tube (i.e., $ER = A_{ET}/A_{PT}$). Here, M_{LSW_2} cannot be obtained from Eq. (12) because M_{b,LSW_2} and M_{LSW_2} are two variables in a single equation. Therefore, an additional equation is necessary to obtain M_{b,LSW_2}. The Mach number behind LSW_2 in the absolute coordinates system in different forms can be expressed as follows:

$$M_{b,LSW_2} = \frac{(\gamma-1)\left(M_{LSW_2}\right)^2}{\sqrt{\left[(\gamma-1)\left(M_{LSW_2}\right)^2 + 2\right]\left[2\gamma\left(M_{LSW_2}\right)^2 - (\gamma-1)\right]}} - \sqrt{\frac{\left[(\gamma-1)\left(M_{LSW_2}\right)^2 + 2\right]}{\left[2\gamma\left(M_{LSW_2}\right)^2 - (\gamma-1)\right]}}. \tag{16}$$

Further details for derivation of Eqs. (12) and (16) have been provided in the Supplementary Material (Supplementary method A). All quantities behind LSW_2 can be predicted from Eqs. (1)–(16).

After LSW_2 reaches the exit of expanded zone, the RSW and LSW_3 are generated owing to the difference in the tube diameter. The RSW propagates to the entrance to the expanded zone, and LSW_3 propagates in an identical direction to the movement of pod. The pressure increases behind RSW because the mass is accumulated owing to the smaller diameter of contraction tube which makes the

restricted structure. The mass flow rates behind RSW were assumed to be identical to the one behind LSW_3. The mass flow rate behind RSW and LSW_3 in the absolute coordinates system can be expressed as follows:

$$\dot{m}_{b,RSW} = \rho_{b,LSW_2}\sqrt{\gamma RT_{b,LSW_2}}\left[\left(2M_{b,LSW_2} - M^s_{a,RSW}\right)\frac{(\gamma+1)\left(M^s_{a,RSW}\right)^2}{(\gamma-1)\left(M^s_{a,RSW}\right)^2+2} - M^s_{a,RSW}\right]A_{ET}, \tag{17}$$

$$\dot{m}_{b,LSW_3} = \rho_{a,LSW_3}\sqrt{\gamma RT_{a,LSW_3}}\left[\frac{(\gamma+1)\left(M^s_{a,LSW_3}\right)^3}{(\gamma-1)\left(M^s_{a,LSW_3}\right)^2+2} - M^s_{a,LSW_3}\right]A_{CT}, \tag{18}$$

where

$$M^s_{a,RSW} = \frac{v_{RSW} - v_{a,RSW}}{\sqrt{\gamma RT_{a,RSW}}}, \tag{19}$$

$$M^s_{a,LSW_3} = \frac{-v_{LSW_3}}{\sqrt{\gamma RT_{a,LSW_3}}}, \tag{20}$$

Here, $\dot{m}_{b,RSW}$ and $\dot{m}_{b,LSW_3}$ are the mass flow rates behind RSW and LSW_3 in the absolute coordinates system. When the mass flow rates behind RSW and LSW_3 are assumed to be identical, there are two variables in one equation. Thus, an additional equation related to $M^s_{a,RSW}$ and M^s_{a,LSW_3} is required to obtain the Mach number solution. It should be noted that the contraction ratio (i.e., expansion-to-contraction tube area ratio; $CR = A_{ET}/A_{CT}$) can be defined from the expansion and contraction tube. The stagnation pressures behind RSW and LSW_3 were assumed to be identical, and are considered as an additional condition because there is no shock wave between RSW and LSW_3. The stagnation pressures behind RSW and LSW_3 in the absolute coordinates system can be expressed as follows:

$$p_{o,RSW} = p_{b,RSW}\left[1 + \frac{\gamma-1}{2}\left(\left(2M_{b,LSW_2} - M^s_{a,RSW}\right)\frac{\sqrt{T_{b,LSW_2}}}{\sqrt{T_{b,RSW}}} - \sqrt{\frac{(\gamma-1)\left(M^s_{a,RSW}\right)^2+2}{2\gamma\left(M^s_{a,RSW}\right)^2-(\gamma-1)}}\right)\right]^{\frac{\gamma}{\gamma-1}}, \tag{21}$$

$$p_{o,LSW_3} = p_{b,LSW_3}\left[1 + \frac{\gamma-1}{2}\left(M^s_{a,LSW_3}\frac{\sqrt{T_{a,LSW_3}}}{\sqrt{T_{b,LSW_3}}} - \sqrt{\frac{\left[(\gamma-1)\left(M^s_{a,LSW_3}\right)^2+2\right]}{\left[2\gamma\left(M^s_{a,LSW_3}\right)^2-(\gamma-1)\right]}}\right)\right]^{\frac{\gamma}{\gamma-1}}. \tag{22}$$

Here, $p_{o,RSW}$ and p_{o,LSW_3} are the stagnation pressures behind RSW and LSW_3, respectively. Further details for derivation of Eqs. (17)–(18) and (21)–(22) have been provided in the Supplementary Material (Supplementary method B).

2.4. Prediction of reflected expansion wave

When LSW_1 reaches the entrance to the expanded zone, the reflected expansion wave (REW) is generated, which then propagates to the pod (as shown in Fig. 2(b)) [27]. The low-pressure field is generated behind the REW, which subsequently results in a decrease in the aerodynamic drag on a pod when REW reaches the pod. Accordingly, the prediction of speed for REW is important because the start time of the decreasing drag can be estimated. The expansion waves spread out according to the time variation with decreasing pressure and increasing velocity [23]. The expansion wave propagates at the speed of sound when the fluid in front of the wave is a stationary. However, the speed of expansion wave is affected when the fluid flows in front of the wave. In the Hyperloop system, the fluid flows owing to the movement of pod, and this flow velocity affects the speed of REW. The flow velocity behind LSW_1 is varied with the BR because the critical Mach number is different according to the cross-sectional area change as shown in Eq. (7). Accordingly, the Mach number of the REW under the isentropic flow can be expressed as follows:

$$M_{REW} = 1 + \frac{2\left[1 - \left(M_{LSW_1}\right)^2\right]}{\sqrt{\left[2\gamma\left(M_{LSW_1}\right)^2 - (\gamma-1)\right]\left[(\gamma-1)\left(M_{LSW_1}\right)^2+2\right]}}. \tag{23}$$

Here, M_{REW} is the Mach number of REW. Further details for derivation of Eq. (23) have been provided in the Supplementary Material (Supplementary method C).

3. Numerical methods

3.1. Assumptions and simulations

In this study, numerical simulations were conducted using a commercial software (ANSYS Fluent). A two-dimensional axisymmetric model was adopted, and unsteady-state and simulations were performed to analyze the impact of sudden expansion and contraction of the tube on the compressible flow phenomena and aerodynamic characteristics. It was assumed that the working fluid was as an air

following the ideal gas law. Furthermore, the air was assumed as a compressible and viscous fluid. Sutherland's model was applied for the fluid viscosity, which is a function of only temperature [28]. The compressible solver was applied because a high Mach number was expected. The Mach number, which classifies an incompressible or compressible flow, is defined as the ratio of flow velocity to speed of sound (c), and the speed of sound is defined as $\sqrt{\gamma RT}$ under the isentropic and ideal gas conditions.

The Reynolds number (Re) is a non-dimensional parameter, and is defined as the ratio of inertial force to viscous force. It can be expressed as $Re = \rho v d_h/\mu$, where d_h (i.e., $d_h = d_{PT} - d_P$) is the hydraulic diameter and μ is the fluid viscosity. In this study, the Reynolds numbers are 20,300, 30,455, 40,600, and 50,760 corresponding to the BR of 0.64, 0.49, 0.36, and 0.25, respectively. Therefore, a turbulent flow is considered in this system. Furthermore, the tube and pod walls were assumed to have smooth surfaces. All numerical simulations were performed for a flow time of 1 s. The time step (Δt) was set to 0.00005 s. The implicit method was applied to calculate the governing equations. The second-order upwind scheme was applied for the flow, turbulent kinetic energy, and the specific dissipation rate. To capture the strong shock, the advection upstream splitting method (AUSM) was applied in all simulations.

3.2. Governing equations

The governing equations for compressible flow consist of the conservation of mass, momentum, and energy equations:

$$\frac{\partial \rho}{\partial t} + \frac{\partial}{\partial x_i}(\rho u_i) = 0, \tag{24}$$

$$\frac{\partial}{\partial t}(\rho u_i) + \frac{\partial}{\partial x_i}(\rho u_i u_j) = -\frac{\partial p}{\partial x_i} + \frac{\partial}{\partial x_j}\left[\mu\left(\frac{\partial u_i}{\partial x_j} + \frac{\partial u_j}{\partial x_i} - \frac{2}{3}\delta_{ij}\frac{\partial u_k}{\partial x_k}\right)\right] + \frac{\partial}{\partial x_j}\left(-\rho u_i' u_j'\right), \tag{25}$$

$$\frac{\partial}{\partial t}(\rho E) + \frac{\partial}{\partial x_j}\left(u_j(\rho E + p)\right) = \frac{\partial}{\partial x_j}\left[\left(k_{eff}\right)\frac{\partial T}{\partial x_j}\right] + \frac{\partial}{\partial x_j}\left[u_i \mu_{eff}\left(\frac{\partial u_i}{\partial x_j} + \frac{\partial u_j}{\partial x_i} - \frac{2}{3}\delta_{ij}\frac{\partial u_k}{\partial x_k}\right)\right]. \tag{26}$$

In this study, the Reynolds number is in the fully turbulent flow regime, as described in section 3.1. Accordingly, the Reynolds averaged Navier Stokes (RANS) equation was solved with the $k-\omega$ shear stress transport (SST) turbulence model [29], which has been widely used for supersonic flow simulation and tube-train or tunnel-train system [30–34]. The direct numerical simulation (DNS) and large eddy simulation (LES) can accurately predict the turbulence [35,36]. However, these simulations are challenging owing to the simulation cost. The $k-\omega$ SST model accurately predicts the shock location and phenomena in the separation region at transonic speed [37–40]. The turbulence model includes the turbulence kinetic energy k and specific rate of dissipation ω as variables:

$$\frac{\partial}{\partial t}(\rho k) + \frac{\partial}{\partial x_j}\left(\rho u_j k\right) = \tau_{ij}\frac{\partial u_i}{\partial x_j} - \beta^* \rho \omega k + \frac{\partial}{\partial x_j}\left[\left(\mu + \sigma_k \mu_t\right)\frac{\partial k}{\partial x_j}\right], \tag{27}$$

$$\frac{\partial}{\partial t}(\rho \omega) + \frac{\partial}{\partial x_j}\left(\rho u_j \omega\right) = \frac{\gamma}{\nu_t}\tau_{ij}\frac{\partial u_i}{\partial x_j} - \beta \rho \omega^2 + \frac{\partial}{\partial x_j}\left[\left(\mu + \sigma_\omega \mu_t\right)\frac{\partial k}{\partial x_j}\right] + 2\rho\left(1 - F_1\right)\frac{\sigma_{\omega 2}}{\omega}\frac{\partial k}{\partial x_j}\frac{\partial \omega}{\partial x_j}, \tag{28}$$

with

$$F_1 = \tanh\left\{\left\{\min\left[\max\left(\frac{\sqrt{k}}{\beta^* \omega y}, \frac{500\nu}{y^2 \omega}\right), \frac{4\rho\sigma_{\omega 2} k}{CD_{k\omega} y^2}\right]\right\}^4\right\}, \tag{29}$$

$$CD_{k\omega} = \max\left(2\rho\frac{\sigma_{\omega 2}}{\omega}\frac{\partial k}{\partial x_i}\frac{\partial \omega}{\partial x_j}, 10^{-20}\right), \tag{30}$$

$$\mu_t = \frac{\rho a_1 k}{\max\left(a_1 \omega, \Omega F_2\right)}, \tag{31}$$

$$F_2 = \tanh\left(\max\left(2\frac{\sqrt{k}}{\beta^* \omega y}, \frac{500\nu}{y^2 \omega}\right)^2\right). \tag{32}$$

Where β^* and σ_k are the closure coefficients in the turbulence kinetic energy equation; β, σ_ω, and $\sigma_{\omega 2}$ are the coefficients in the specific dissipation rate equation, and μ_t is the turbulence viscosity.

3.3. Computational domain and boundary conditions

In the Hyperloop system, the shape of the pod is important for the aerodynamic characteristics and pressure waves. However, in this study, the shape of pod was assumed as an idealized hemispherical model for the nose and tail to focus on the general physics of compressible flow phenomena and aerodynamic characteristics, excluding the effects of shape. To investigate the general flow fields in the Hyperloop system, the idealized model has been used in previous studies [10,15]. Therefore, a two-dimensional axisymmetric model was applied in all simulations. Fig. 3(a) presents the schematic of geometric model applied in this study with x-y coordinates. When the pod travels in the tube, the cross-sectional area around the nose and tail of pod changes. The cross-sectional area between the tube and the pod is similar to that of the converging-diverging nozzle because the shape of the nose and the tail is a hemisphere. A convergent section and a divergent section are formed around the nose and tail of pod, respectively. The straight section, which is unchanged cross-sectional area, is formed between the nose and tail of pod.

The total lengths of the tube and pod were set to 1129 and 43 m, respectively. The length of the tube was sufficient to prevent a numerical instability because the pressure waves such as compression and expansion waves induced by the pod propagate to the end of

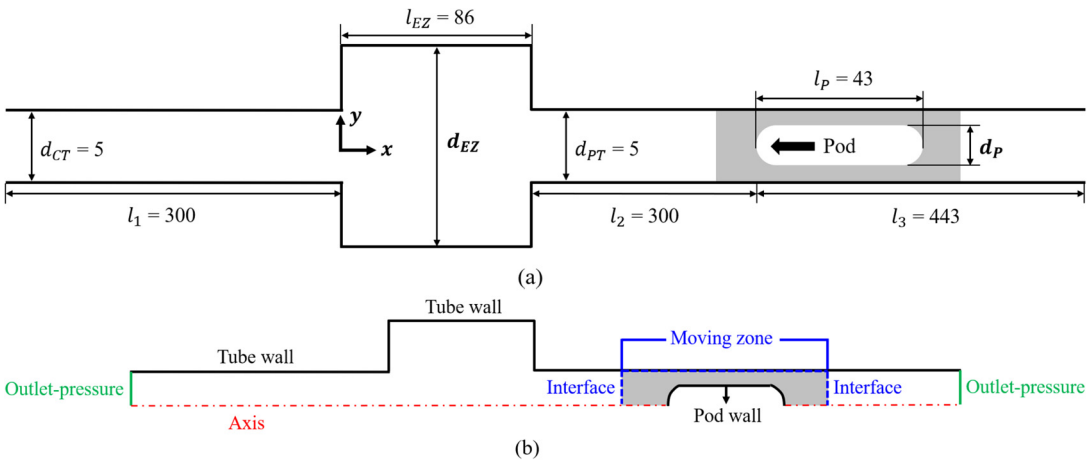

Fig. 3. Schematic of (a) geometric model (unit: m) and (b) boundary conditions. Diameter of primary tube (d_{PT}) and contraction tube (d_{CT}) are 5 m, and those of pod (d_P) are 2.5, 3, 3.5, and 4 m corresponding to BR 0.25, 0.36, 0.49, and 0.64, respectively. Diameters of expanded zone (d_{EZ}) are 6, 8, 10 m in correspondence to ER 1.44, 2.56, and 4, respectively; CR is identical in this study. Black arrow in (a) indicates moving direction of pod. Gray area represents moving zone.

tube. The distance between the entrance to the expanded zone and the pod nose was set to 300 m, and the pod moves to left until the simulation time of 1 s at a speed of 300 m/s. Therefore, the simulation was performed until the pod locates the entrance to the expanded zone. Note that, the pod instantly starts for the movement. A previous study observed that the instant start and gradual acceleration of the pod are insignificant [15]. The shape of expanded zone was assumed as an idealized cylinder to investigate the general flow physics of the sudden expansion and contraction. The diameters of primary and contraction tubes (d_{PT} and d_{CT}) were set to 5 m. Furthermore, the diameters of pod were 2.5, 3, 3.5, and 4 m corresponding to the BR of 0.25, 0.36, 0.49, and 0.64, respectively. The diameters of expanded zone (d_{EZ}) were set to 6, 8, and 10 m corresponding to the ERs and CRs of 1.44, 2.56, and 4, respectively. The length of the expanded zone (l_{EZ}) was set to 86 m, which corresponded to twice that of the length of pod ($2l_P$).

Fig. 3(b) presents the boundary conditions applied in this study. The outlet-pressure was applied at the ends of the tube as outlet conditions with the pressure of 101.325 Pa (1/1000 atm) and temperature of 300 K. The walls of the primary, expansion, and contraction tubes were the stationary walls with adiabatic and no-slip conditions. To simulate the movement of the pod, a moving zone was generated with length of 80 m. The length of the moving zone was sufficient to prevent the numerical instabilities that are caused by the compressible flow behaviors around the interfaces. The wall of the pod was set as the moving wall with adiabatic and no-slip conditions. The wall of the pod moves along the moving zone at a speed of 300 m/s in all simulations. An initial solution of pressure, temperature, and velocity for the flow field is 101.325 Pa, 300 K, and zero, respectively.

3.4. Computational grid

The overset mesh method for a dynamic mesh was applied to the computational grid. This method has been widely adopted for a moving object owing to several advantages [41–44]. The overset mesh consists of a background and component mesh. The background and component mesh are stationary and moving zones, respectively. There is no re-meshing process because the component mesh overlaps the background mesh, and moves on this background mesh. Therefore, the overset mesh method provides accurate solutions and reduces the simulation time because the quality of mesh is preserved and generating time is not required. In this method, the background and component mesh coexist around the pod containing the interfaces. The cell data was interpolated at the interface where the part of background and component mesh overlapped to transfer the numerical data between two meshes [45,46].

In this study, the tube mesh (as background) and the moving zone mesh (as component) were generated to apply the overset mesh method. Fig. 4 shows the computational grid for the component and background mesh. The background and component mesh were hexahedral type. A fine mesh was generated near the walls of the tube and pod for the component mesh and background mesh (as shown in Fig. 4), because a large velocity gradient was expected owing to the viscosity effects such as an aerodynamic boundary layer. The number of grid nodes for the component mesh was 532,854 in the BR of 0.64, and the first cell height from the walls of the tube and the pod was set to 0.0001 m, considering the dimensionless first cell height (y^+) is less than 1, to obtain the accurate solution with the adopted RANS model. The fine mesh was generated around the expansion and contraction region (as shown in Fig. 4(b)) because the large variation in flow quantities was expected. The number of grid nodes for the background mesh was 617,148 in the expansion ratio 4 (ER = 4), and the first cell height was set to 0.001 m. The result of a grid independence test is presented in section 4.1.

4. Results and discussion

4.1. Grid independence test

To obtain an accurate solution, the grid independence test was performed. The BR of 0.64 was adopted for the grid independence test. In the Hyperloop system, the intensity of shock waves and flow quantities is more severe for a higher BR. The number of grid nodes was set to 378,004, 532,854, and 687,704, only for the component mesh. The ER value (i.e., CR) of 4 was adopted for the background mesh. The number of grid nodes for the background mesh including moving pod was set to 617,148. The drag coefficient (C_d) was compared according to the number of grid nodes. The drag coefficient can be expressed as follows:

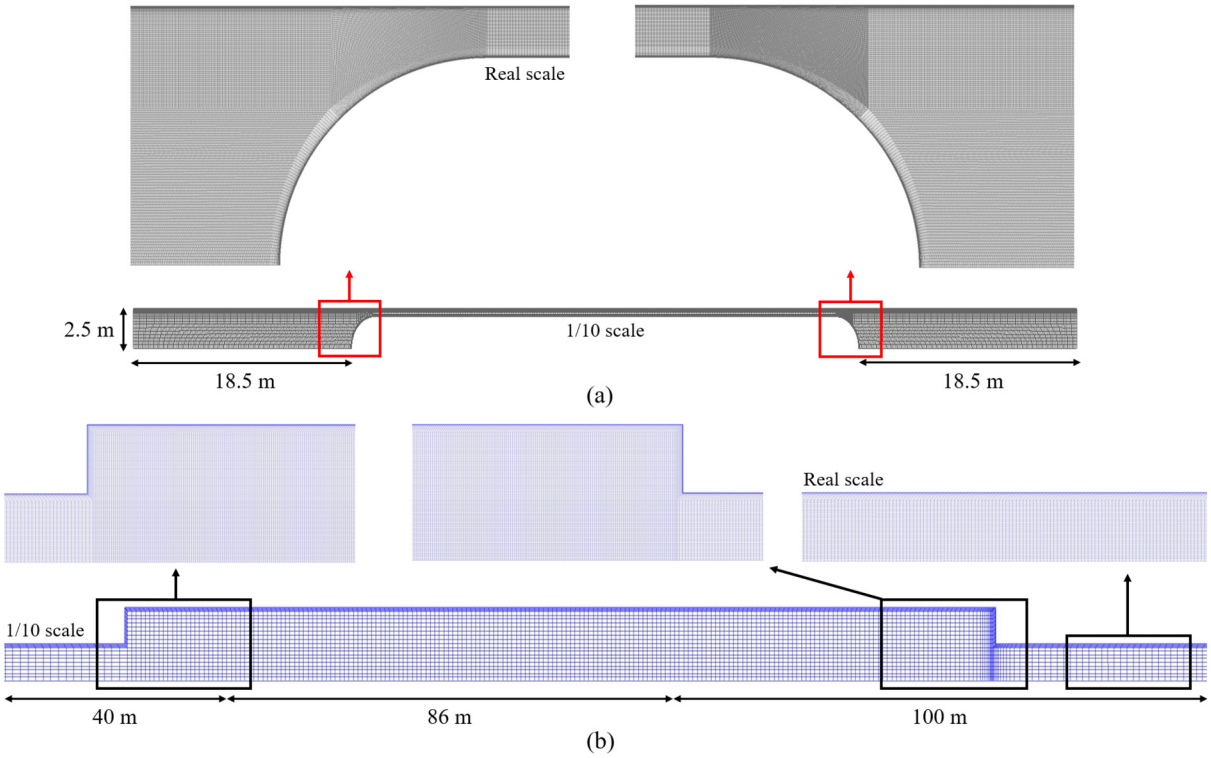

Fig. 4. Computational grid for (a) component (moving zone) mesh and (b) background (tube) mesh. Size of mesh in this figure is scaled by a factor 10 in both horizontal and vertical directions, except in magnified views. Magnified views are an original scale.

$$C_d = \frac{F_d}{\frac{1}{2}\rho_\infty v_p A_p}. \tag{33}$$

Here, F_d is the drag force and A_p is the frontal area of pod. The drag coefficients for coarse, medium, and fine mesh were calculated as 1.765, 1.743, and 1.743, respectively. Fig. 5 presents the normalized pressure distribution with respect to the number of grid nodes a simulation time of 1 s. Here, the normalized pressure was calculated from the static pressure divided by the tube density (ρ_∞) and speed of sound (c_∞). The fluid density is 0.001177 kg/m^3, and the speed of sound is 347.22 m/s corresponding to a temperature of 300 K. The total number of grid nodes for the coarse, medium, and fine mesh were 995,152, 1,150,002, and 1,304,852, respectively. In the magnified views, the relative error for the normalized pressure of coarse and medium mesh was 1.26%. On the other hand, the normalized pressures of medium and fine mesh have a similar value with a relative error of 0.26%. Therefore, the number of grid nodes of medium mesh (1,150,002) was adopted for the BR of 0.64 in the total mesh. The number of grid nodes for the BRs of 0.25, 0.36, and 0.49 were adopted with a similar level of the medium mesh.

4.2. Normal shock wave and pressure field

As mentioned in section 2.1, the high-pressure and low-pressure fields are generated by the movement of the pod. Thus, the LSW_1 with the high-pressure magnitude propagates in the direction of the pod movement. Fig. 6(a) presents the normalized pressure distribution with LSW_1 for BR = 0.36 and ER = 2.56 at t = 0.6 s. The high-pressure region is formed between LSW_1 and nose of the pod, and the low-pressure region develops owing to the oblique shock wave. The oblique shock wave develops because the choked flow occurs in the straight section between the tube and pod for the pod speed of 300 m/s in this study. Once the oblique shock wave develops, the pressure decreases rapidly and the velocity increases. The oblique shock wave is reflected to the wall of tube; the symmetric shock wave structure is formed because the pod was assumed as an idealized hemisphere shape. Once LSW_1 reaches the entrance to the expanded zone, REW and LSW_2 are generated in different direction (as shown in Fig. 6(b)). The LSW_2 is generated when the flow from the primary tube is fully developed in the expanded zone. The pressure magnitude of LSW_2 is lower than that of LSW_1 because the expanded area is larger than that of primary tube. During the expansion, the pressure decreases before the flow is fully developed. In other words, the flow accelerates near the expansion as mentioned in previous study [27]. In the primary tube, the pressure decreases in the region after REW propagates. When REW reaches the pod, the aerodynamic drag is affected; the aerodynamic drag decreases by the lower pressure owing to the REW than that behind LSW_1. The details of aerodynamic drag coefficient are discussed in section 4.4. After LSW_2 reaches the entrance to the contraction tube (i.e., the end of expanded zone), the RSW and LSW_3 are generated, and they propagate in different directions. A higher pressure is formed behind RSW because the mass flow accumulates owing to the conjunction of expansion and contraction tube. The density and pressure increase, and the flow velocity decreases behind RSW. The RSW propagates to the entrance to the expanded zone, which may increase the pressure in the entire expanded zone during propagation. In the contraction tube, the pressure increases behind LSW_3 which propagates with a high-pressure magnitude. Around the nose of pod, the pressure decreases in Fig. 6(c) compared with the Fig. 6(a)–6(b) because REW has already reached the pod.

The normal shock wave and pressure field are quantitatively analyzed. Fig. 7 presents the normalized pressure distribution for the BR of 0.36 and ER of 2.56 at the time of 0.55 and 0.6 s. When the pod moves in the subsonic speed, LSW_1 propagates with the high-pressure

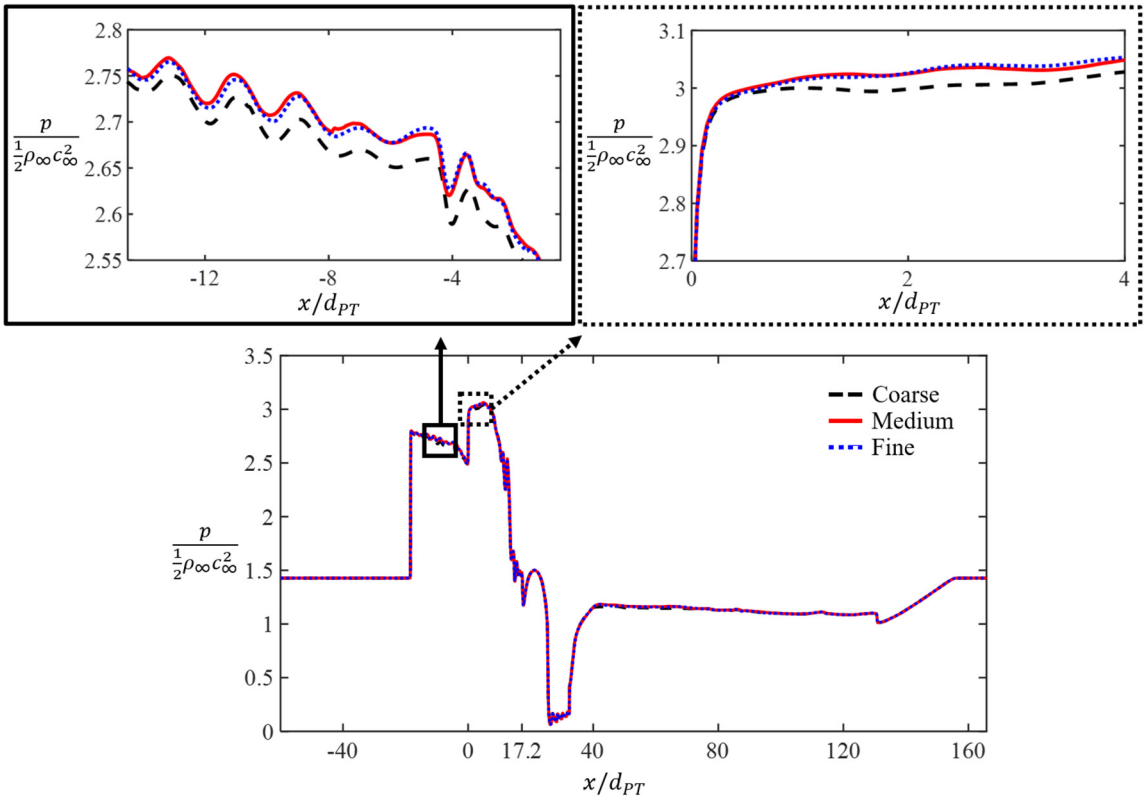

Fig. 5. Normalized pressure with respect to number of grid nodes for grid independence test. Computational grids for coarse (995,152 nodes), medium (1,150,002 nodes), and fine (1,304,852 nodes) mesh were compared. Magnified views show difference in normalized pressure for these meshes. BR and ER are 0.64 and 4 for grid independence test.

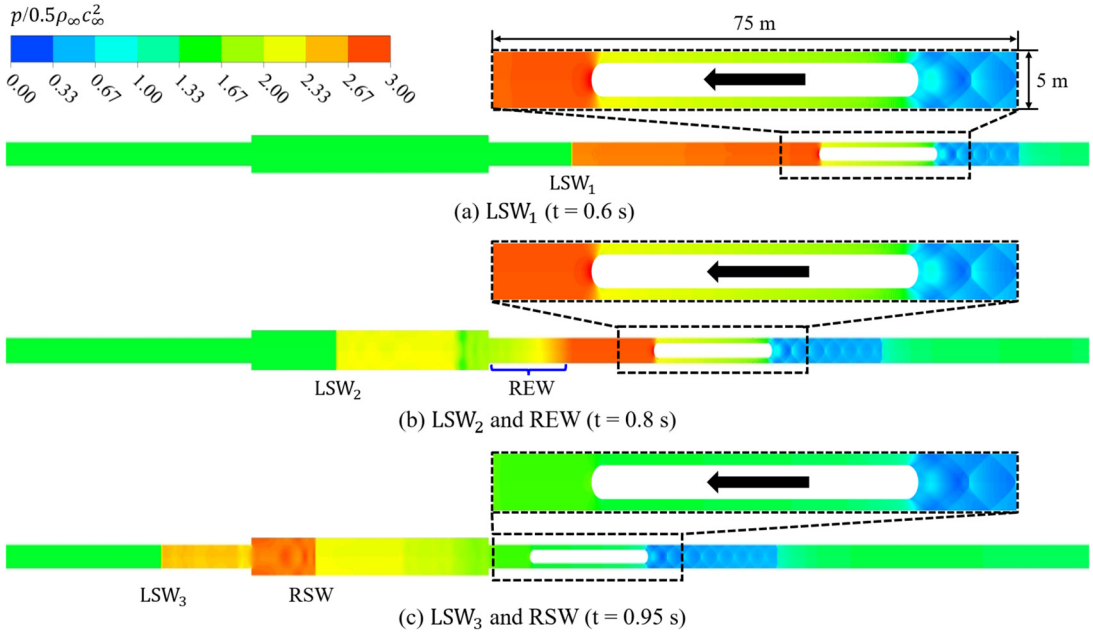

Fig. 6. Normalized pressure distribution according to development of pressure waves. (a) LSW_1 at t = 0.6 s, (b) LSW_2 and REW at t = 0.8 s, and (c) LSW_3 and RSW at t = 0.95 s represent pressure waves in sudden expansion and contraction of tube. Diameter of pod is 3 m corresponding to BR = 0.36, and that of expanded zone is 8 m corresponding to ER = 2.56. Magnified view shows flow around pod.

magnitude. Owing to LSW_1, the discontinuous change in the local quantities occurs across the normal shock wave. From the nose and tail of the pod, the pressure decreases because the flow experiences the convergent and divergent sections between the tube and pod. The choked flow occurs for all BR covering this study, and the flow behavior is identical with respect to the BR. In the divergent section between the tube and pod, the flow accelerates, and the pressure rapidly decreases with the oblique shock wave.

A magnified view of the normalized pressure distribution at 0.7 and 0.75 s is shown in Fig. 8. Once LSW_1 reaches the entrance to the expanded zone, LSW_2 and REW are generated. The LSW_2 propagates inside the expanded zone with increasing pressure, and a low-pressure field is formed around the entrance to the expanded zone owing to the flow acceleration. The pressure behind the normal shock

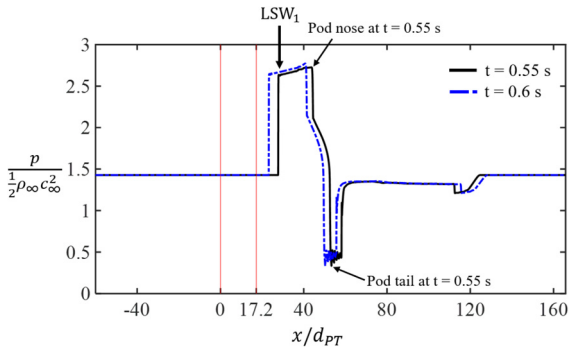

Fig. 7. Normalized pressure distribution for BR = 0.36 and ER = 2.56. Black arrows indicate LSW_1 and locations of nose and tail of pod at t = 0.55 s. Red lines indicate entrance and exit of expanded zone. (For interpretation of the colors in the figure(s), the reader is referred to the web version of this article.)

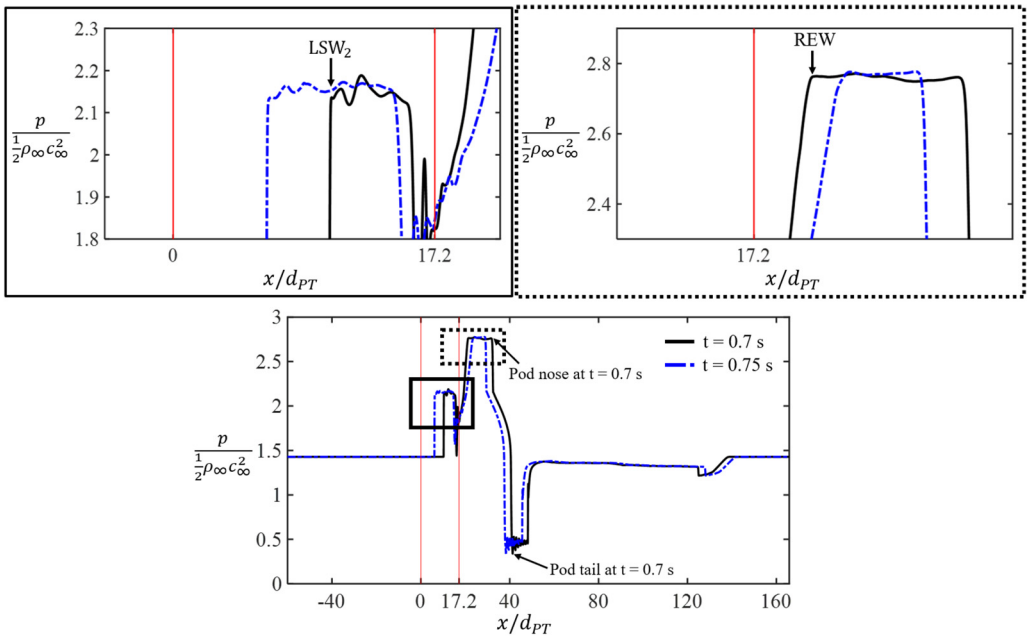

Fig. 8. Normalized pressure distribution for BR = 0.36 and ER = 2.56.

wave is lower than that behind LSW_1 because the cross-sectional area of the expanded zone is larger than that of the primary tube. Accordingly, the cross-sectional area of the expanded zone is a primary factor in the flow quantities. From the magnified view with LSW_2, the pressure profile has an oscillatory form owing to the wave reflection at the wall of expanded zone. In the primary tube, the REW propagates to the pod as the pressure decreases. Thus, the pressure between the entrance to the expanded zone and REW has a gradual profile as a characteristic of the expansion wave.

Once LSW_2 reaches the entrance to the contraction tube, RSW and LSW_3 are generated, and they propagate in opposite directions (as shown in Fig. 9). Because LSW_2 reflects off the entrance to the contraction tube, the RSW with a high pressure is generated. At t = 0.95 s, the pressure in front of the pod evidently decreases owing to the effect of REW. In the contraction tube, LSW_3 propagates with the high-pressure field. Accordingly, the cross-sectional area of the contraction tube is a key factor that determines the pressure magnitude and propagation speed of LSW_3.

4.3. Aerodynamic drag

The aerodynamic drag was analyzed based on the numerical simulation. When the pod moves at a transonic speed, the high-pressure and low-pressure fields are generated owing to the normal shock wave and oblique shock wave. Accordingly, the drag coefficient increases with the intensities of the normal shock wave and oblique shock wave. The variation of drag coefficient from t = 0.2 s to t = 1 s with respect to the BR is presented as shown in Fig. 10(a). The drag coefficient increases with the BR because the pressure on the nose of the pod increases. For the nozzle relation, shown in Eq. (7) under choking condition, the critical Mach number (i.e., Mach number of subsonic solution) is lower for a higher BR in the pod-fixed coordinates system. Furthermore, the stagnation pressure at the front of pod is higher for a high BR. Accordingly, the pressure in front of pod is higher for a high BR, and the drag coefficient increases. As mentioned above, as LSW_1 reaches the entrance to the expanded zone, the REW propagates to the pod, and the aerodynamic drag coefficient decreases when REW reaches the pod, referred to as the REW effect (as shown in Fig. 10(a)). Because of the characteristic of a REW which decreases the pressure, the pressure distributed on the nose of pod also decreases. Although the propagation Mach numbers of LSW_1 and REW (as presented in Fig. 14) are different, the arrival times of REW for all BRs are similar. Additionally, the minimum drag coefficients owing to REW are similar for all BR. In other words, the rate of decrease of the drag coefficient increases with an increase in BR, and the REW effect

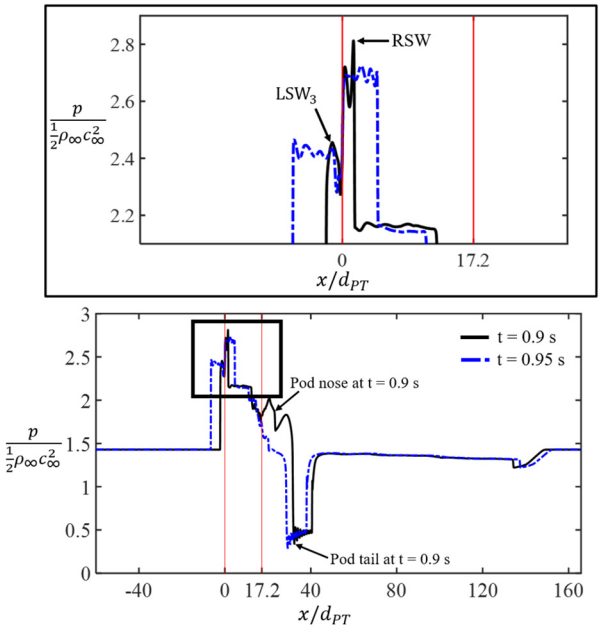

Fig. 9. Normalized pressure distribution for BR = 0.36 and ER = 2.56.

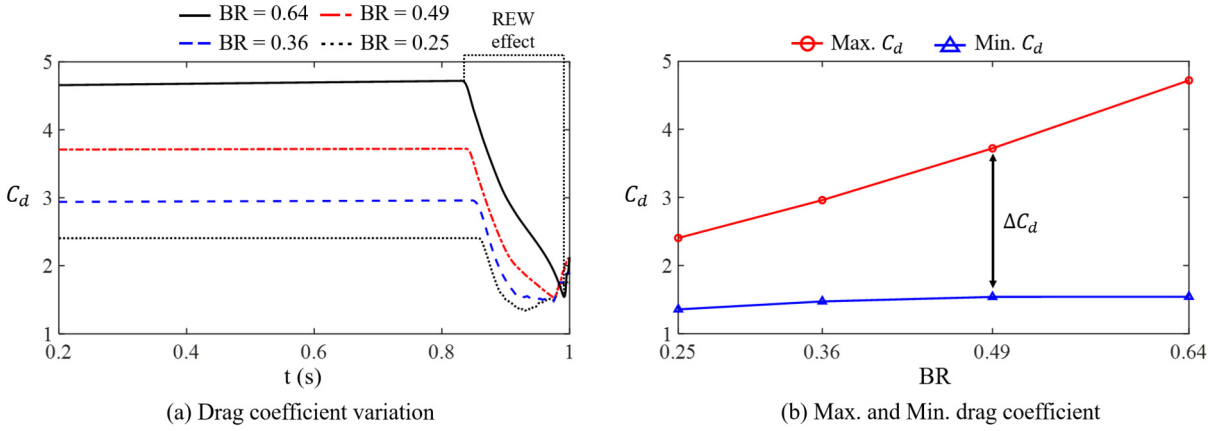

(a) Drag coefficient variation (b) Max. and Min. drag coefficient

Fig. 10. (a) Drag coefficient variation according to time and (b) maximum and minimum drag coefficient with respect to blockage ratio (BR). ΔC_d is difference between maximum and minimum drag coefficient with respect to blockage ratio.

is significant for a high BR. More specifically, the drag coefficient initially increases when the REW reaches the pod. However, the drag coefficient increases near the entrance of the expanded zone, regardless of the BR. The drag initially decreases because REW decreases the pressure on the nose of pod. After REW propagates between the tube and the pod, it reaches the tail of pod. When the REW reaches the tail of the pod, REW also decreases the pressure on the tail. Accordingly, the drag coefficient increases when the REW reaches the tail of the pod. Because the propagation speed of the REW is different for different BRs, the minimum drag coefficient is observed at a different time with respect to the BR. The maximum drag coefficient occurs before the REW reaches the pod, and the minimum drag coefficient occurs after the REW reaches the pod. As mentioned above, the maximum drag coefficient before REW reaches the pod increases with the increase in BR. However, the minimum drag coefficient with the REW effect is similar regardless of the BR (as shown in Fig. 10 (b)). This result shows that when sudden expansion and contraction exist in the tube, the drag coefficient with REW effect has a similar value, regardless of the BR. Therefore, the difference between the maximum and minimum drag coefficients increases with an increase in BR.

4.4. Effects of blockage, expansion, and contraction ratio

The local quantities, such as density, pressure, temperature, and flow velocity, vary with respect to the blockage, expansion, and contraction ratios. Fig. 11 presents the normalized pressure distribution for the expansion ratio of 2.56 with respect to the BR at t = 0.5 s. When the pod moves in the confined tube, LSW_1 propagates regardless of the BR at a pod speed of 300 m/s. The pressure magnitude of LSW_1 increases with the BR. From the comparison of the pressure behind LSW_1 for the BRs of 0.25 and 0.64 under the expansion ratio of 2.56 at a pod speed of 300 m/s, the pressure magnitude for the BR of 0.64 is greater by approximately 32% than that for BR of 0.25. Accordingly, the propagation speed of LSW_1 increases owing to the normal shock wave relation. Behind the tail of pod, the oblique shock wave is symmetrically formed owing to the wall of tube. The oblique shock wave results in a low-pressure field, which results in an increase in the aerodynamic drag. The intensity of oblique shock wave increases with the BR. In other words, the pressure behind the pod decreases with an increase in BR.

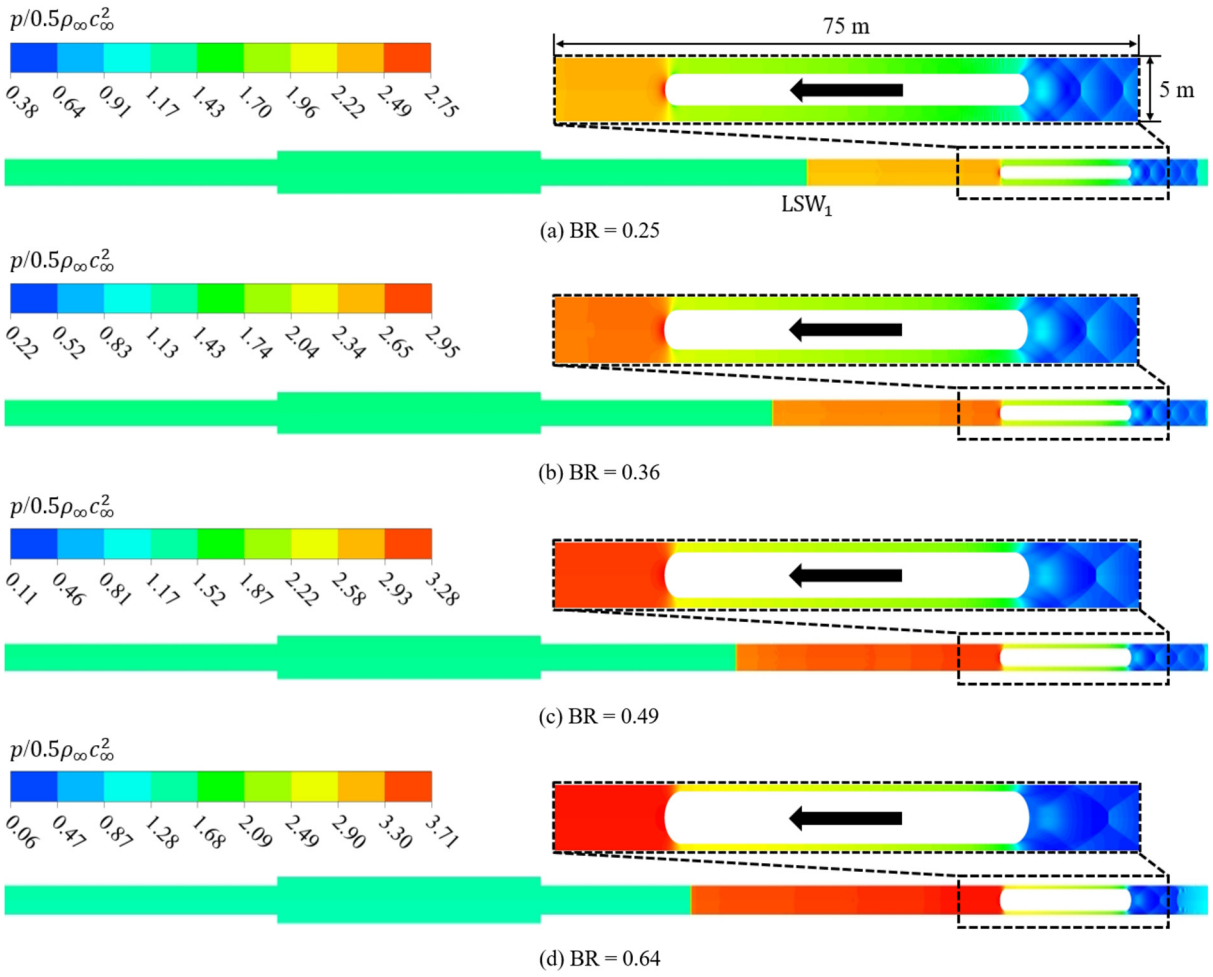

Fig. 11. Normalized pressure distribution with respect to blockage ratio (BR) represented by LSW_1 at 0.5 s. Diameter of expanded zone is 8 m corresponding to ER = 2.56. Magnified view presents flow around pod.

The normalized pressure distribution for the expansion ratio of 2.56 with respect to the BR at t = 0.75 is presented as shown in Fig. 12. The REW and LSW_2 are observed in Fig. 12. In the primary tube, the pressure in front of the pod is increases with the BR, as mentioned above. With the increasing BR at a same speed of pod, the stagnation pressure and the flow velocity increase. Accordingly, the propagation speed of REW decreases owing to the flow velocity in front of REW (i.e., flow velocity behind LSW_1). However, because the propagation speed of LSW_1 is higher with increasing the blockage ratio, REW is generated earlier. Thus, the REW is propagated relatively more, as shown in Fig. 12. In the expanded zone, the pressure magnitude of LSW_2 increases with an increase in BR. Furthermore, the propagation speed of LSW_2 increases with an increase in BR owing to higher pressure ratio in front of and behind LSW_2.

Once LSW_2 reaches the entrance to the contraction tube, the normalized pressure distribution at t = 0.95 s is presented as shown in Fig. 13. The pressure magnitude of the RSW and LSW_3 increase with the increase in BR because the pressure behind LSW_2 increases with an increase in BR. Accordingly, the propagation speed of LSW_3 increases with an increase in BR. However, the propagation speed of the RSW decreases with the increase in BR. Because the propagation of pressure wave is affected by the flow velocity in front of the normal shock wave, the propagation speed is a function of the pressure ratio across the RSW and the flow velocity in front of the RSW (i.e., flow velocity behind LSW_2). Therefore, the propagation speed of RSW decreases with an increase in BR in the same expansion ratio.

The propagation speeds of LSW_1 and REW were predicted through the theoretical consideration in section 2. These speeds can be determined from BR and speed of pod, as shown in Eqs. (7)–(8), and (23). Accordingly, the local quantities behind LSW_1 and the propagation speed of LSW_1 and REW can be predicted for the BR and speed of pod under choked flow. It should be noted that the speed of pod was fixed at 300 m/s in this study; the choked flow occurred in all BRs. Fig. 14 presents the propagation speed as a Mach number for LSW_1 and REW, respectively. Furthermore, the normalized pressure magnitude of LSW_1 is presented in Fig. 14. The propagation speed of LSW_1 increases with an increase in BR. However, the propagation speed of the REW decreases with an increase in BR. The speed of REW is affected by the flow velocity in front of the expansion wave. The directions of the REW and flow in front of the expansion wave are opposites. Because the flow velocity in front of REW increases with the higher BR, the propagation speed of REW decreases. From the comparison of the Mach number of LSW_1 and REW from the simulation and theory, the predicted Mach number is in good agreement. The pressure magnitude of LSW_1 increases with the higher BR because the area between the tube and the pod decreases. The predicted pressure is in good agreement with the simulation results.

Fig. 15 presents the Mach number for the propagation speed and normalized pressure of LSW_2 with respect to the BR and ER. The Mach number and normalized pressure of LSW_2 increase with the higher BR and with a decrease in ER. The propagation speed and normalized pressure of LSW_2 were predicted from Eqs. (1)–(16). To predict the Mach number and normalized pressure, the mass flow rate at the entrance to the expanded zone and behind LSW_2 was assumed to be identical. Accordingly, the equation of compressible mass

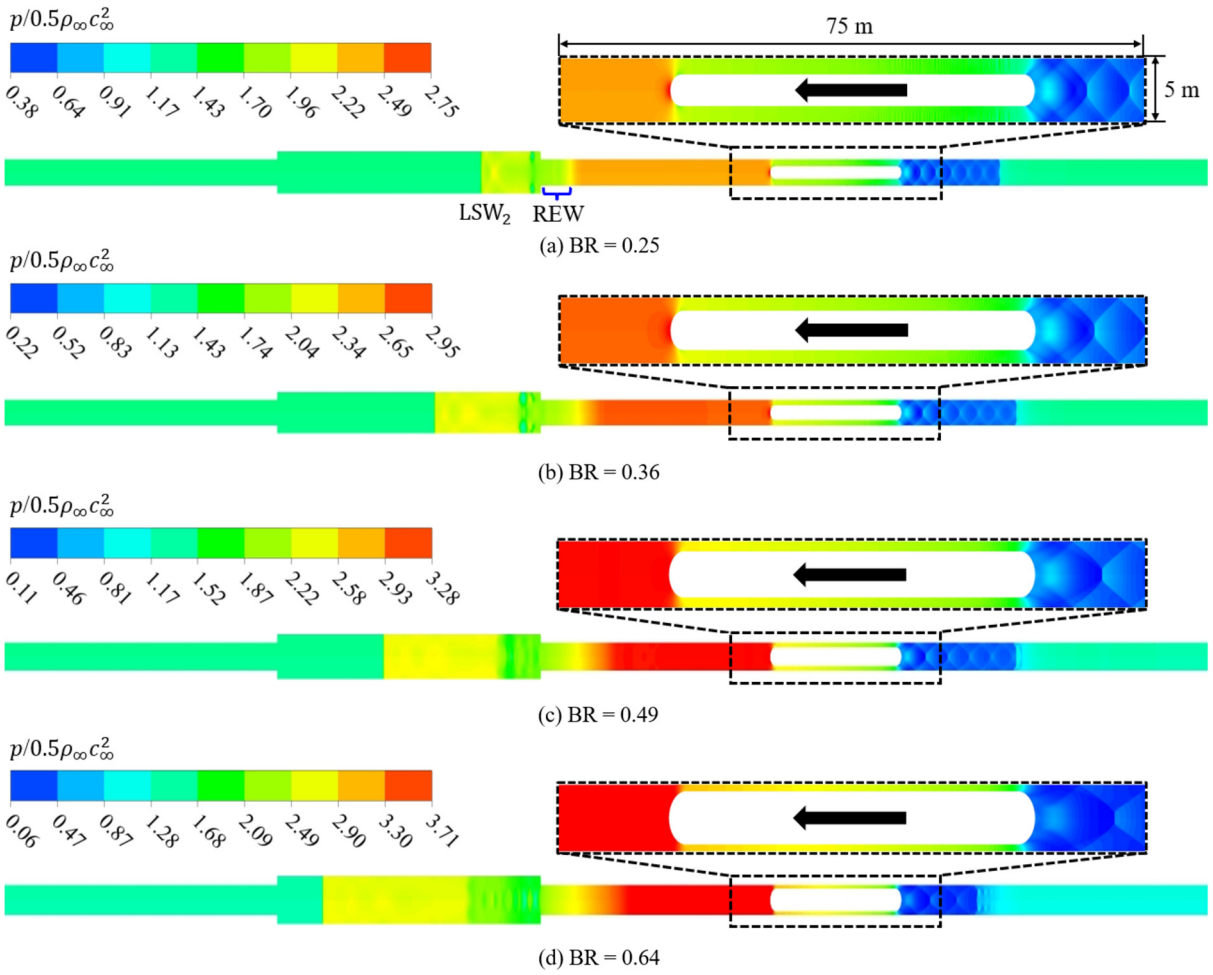

Fig. 12. Normalized pressure distribution with respect to BR represented by LSW_2 and REW at 0.75 s. Diameter of expanded zone is 8 m corresponding to ER = 2.56. Magnified view presents flow around pod.

flow (as shown in Eq. (11)) was calculated under the choking condition at the entrance to the expanded zone. From the comparison of the Mach number and normalized pressure from the theory and simulation, it is observed that a few of errors occur owing to the assumption of the choking condition, 1-D, and frictionless. Eq. (11), the equation of compressible mass flow rate, includes the Mach number at the entrance of the expanded zone, assuming a choked flow. However, because the complex flow around the entrance to the expanded zone occurs owing to the flow separation and recirculation zone, the choking assumptions induce the error between the theoretical and simulation results. Because LSW_1 passes through the entrance of the expanded zone, the fluid flows in the expanded zone that has a larger cross-sectional area than that of the primary tube. Because of the area change, the flow accelerates at the entrance of the expanded zone. However, the accelerating Mach number is different for the BR and ER. Although the Mach number at the entrance of the expanded zone is assumed to be one in the theoretical consideration, this Mach number is not reached for a low ER in the simulation. On the other hands, the Mach number at the entrance of the expanded zone reaches one for the high ER in the simulation. Accordingly, the predicted Mach number and normalized pressure is matched well for the high ER with the low BR. However, the predicted Mach number and normalized pressure are not matched well for the high ER and BR. Although the Mach number at the entrance of the expanded zone reaches one for high ER and BR, the predicted flow velocity behind LSW_1 is overestimated in the theory. Therefore, the predicted Mach number and normalized pressure are overestimated for high ER and BR. In other words, the predicted Mach number and normalized pressure agreed well for the high ER and low BR, and those for the low ER and high BR agreed well owing to the predicted mass flow rate and flow velocity (i.e., the stagnation pressure and temperature). The maximum relative errors between the theory and simulation were 6 and 11% for Mach number and normalized pressure, respectively. These relative errors can be considered in a reasonable range where the prediction with the theory is applicable.

Fig. 16 presents the propagation Mach number and normalized pressure magnitude of RSW and LSW_3 in the absolute coordinates system with respect to the BR and CR. The propagation Mach number of RSW decreases with an increase in BR because the flow velocity in front of RSW increases. Furthermore, the Mach number increases with the higher CR because the pressure behind RSW increases; the pressure ratio behind and in front of RSW increases with the CR at identical BR. The propagation Mach number of LSW_3 increases with the higher BR because the pressure behind LSW_3 increases. Furthermore, the Mach number of LSW_3 increases with the decrease in CR owing to the pressure behind LSW_3. A large relative error was observed between the theoretical and simulation results, and the maximum relative error was approximately 15%. In the theoretical consideration, the quasi-one-dimensional and isentropic flows were assumed to simplify the compressible flow phenomenon. However, the two-dimensional model and viscous fluid were adopted in the numerical simulation. Furthermore, the sudden expansion and contraction generate the recirculation zone with the flow separation. Specifically, in the sudden expansion, the flow separation occurs at the corner of the entrance to the expanded zone. In the sudden contraction, the flow

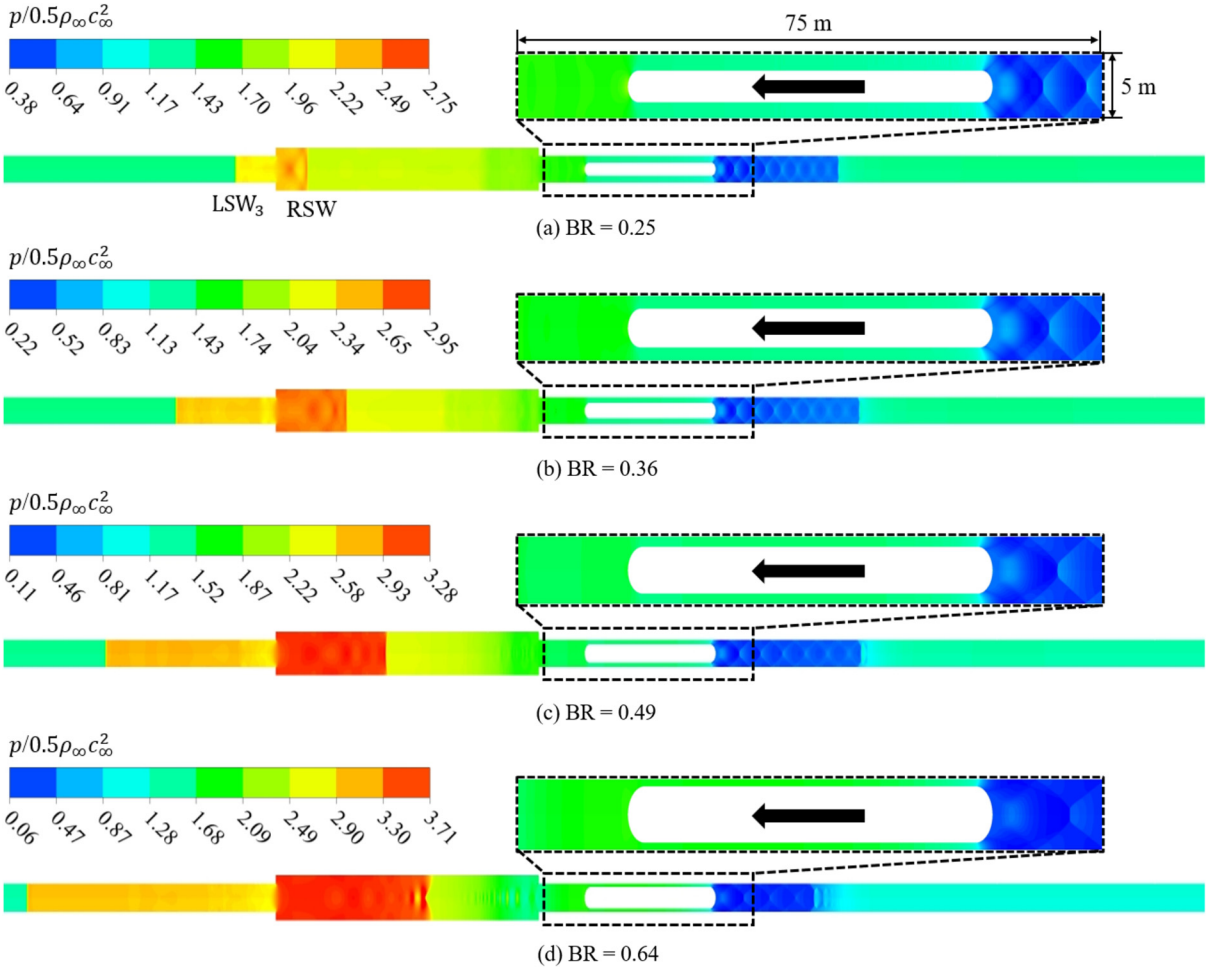

Fig. 13. Normalized pressure distribution with respect to BR represented by LSW_3 and RSW at 0.95 s. Diameter of expanded zone is 8 m corresponding to CR = 2.56. Magnified view shows flow around pod.

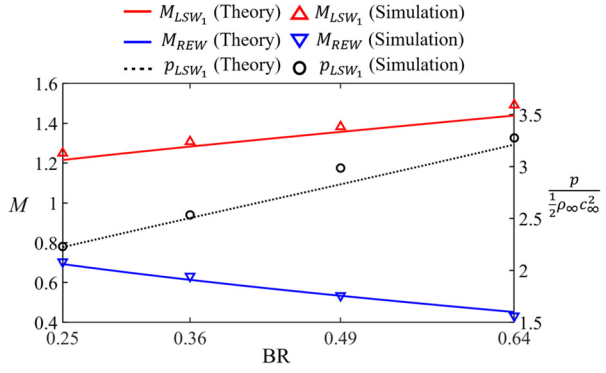

Fig. 14. Mach number (M_{LSW_1}) and normalized pressure magnitude of LSW_1, and Mach number of REW (M_{REW}) with respect to BR. Red and blue solid lines indicate M_{LSW_1} and M_{REW} from theory. Black dotted line indicates normalized pressure magnitude. Red triangle and blue inverse-triangle indicate M_{LSW_1} and M_{REW} from simulation result. Black circle indicates normalized pressure magnitude from simulation results.

separation occurs in the contraction tube. These phenomena were not considered in the theoretical analysis; therefore, the error between the theoretical and simulation results occurred. In the theoretical consideration, the conservations of the mass flow rate and stagnation pressure behind the RSW and LSW_3 were assumed to be identical. However, because of the complex flow field under the two-dimensional axisymmetric model and viscous fluid, the stagnation pressure behind the RSW and LSW_3 did not agree well. Accordingly, the predicted propagation Mach number and normalized pressure of the RSW and LSW_3 did not agree well. Although the difference between the theory and simulation were observed in this study, the presented theory has advantages such as a quick prediction of the propagation Mach number and normalized pressure for each normal shock wave.

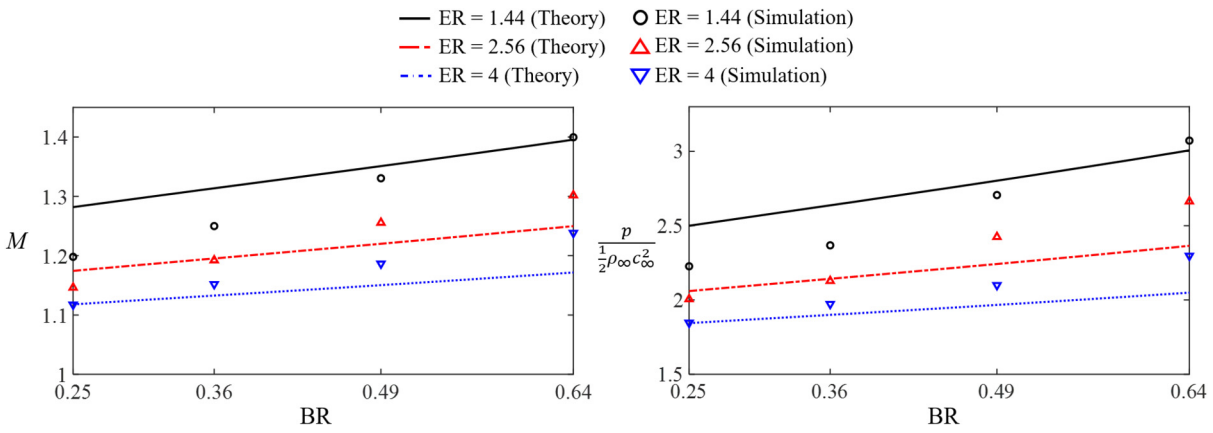

Fig. 15. Mach number (M_{LSW_2}) and normalized pressure of second leading shock wave with respect to BR and ER. Black solid, red single-dotted, and blue dotted lines represent ER of 1.44, 2.56, and 4 from theory, respectively. Black circle, red triangle, and blue inverted-triangle represent ER of 1.44, 2.56, and 4 from simulation, respectively.

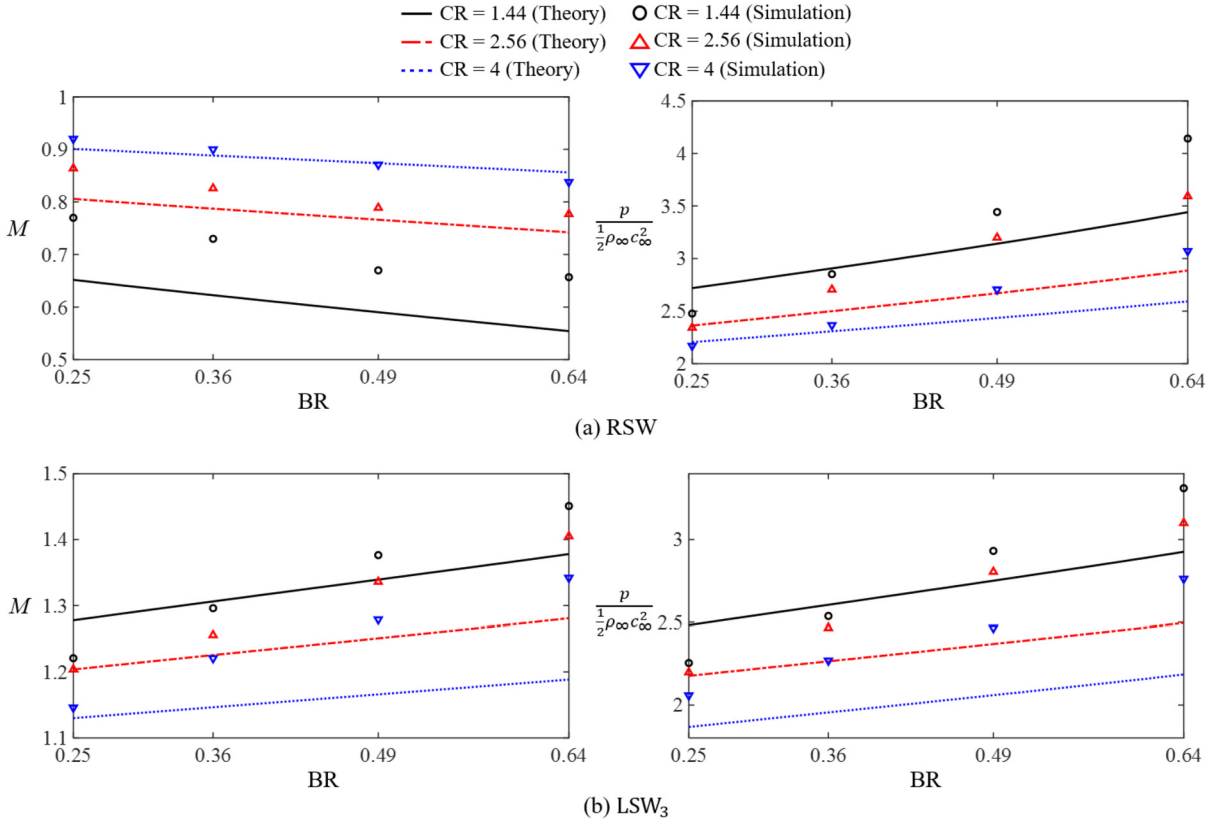

Fig. 16. Mach number and normalized pressure with respect to BR and CR; (a) reflected shock wave (M_{RSW}) and (b) third leading shock wave (M_{LSW_3}). Line configuration is identical to Fig. 15.

5. Conclusion

The effects of sudden expansion and contraction of the tube on compressible flow phenomena in the Hyperloop system were analyzed by conducting a 2D, axisymmetric, and unsteady-state simulation and a theoretical quasi-one-dimensional consideration. The analysis was conducted for various BRs (i.e., BR = 0.25, 0.36, 0.49, and 0.64) and ERs (i.e., ER = 1.44, 2.56, and 4). The pressure waves were classified as LSW$_1$, REW, LSW$_2$, RSW, and LSW$_3$. When the pod moves at a transonic speed, LSW$_1$ with high pressure is generated in front of the pod. Once the LSW$_1$ reaches the entrance to the expanded zone, LSW$_2$ and REW are generated, and they propagate in opposite directions. When LSW$_2$ reaches the entrance to the contraction tube, LSW$_3$ and RSW are generated, and they propagate subsequently. The pressure waves such as normal shock wave and expansion wave change the local quantities in flow fields.

For higher BRs, the propagation Mach number and pressure magnitude of LSW$_1$ increase because the mass flow is accumulated. However, the propagation Mach number of REW decreases with an increase in BR because the flow velocity in front of REW increases. The propagation Mach numbers of LSW$_1$ and REW were successfully predicted under the choking and isentropic flow assumptions compared to the simulation results.

When LSW$_2$ propagates in the expanded zone, the propagation Mach number and pressure magnitude decreases compared to LSW$_1$. The propagation Mach number of LSW$_2$ increases with the BR owing to the higher pressure behind LSW$_2$. However, the propagation Mach

number of LSW_1 decreases with the increase in ER because the pressure behind LSW_2 decreases owing to the larger expansion area. The prediction of propagation Mach number and pressure magnitude of LSW_2 was performed under choked flow at the entrance to the expanded zone and identical mass flow rate conditions. It is seen that the predicted and simulated results are in good agreement.

Once LSW_2 reaches the entrance to the contraction tube, LSW_3 and RSW propagate in opposite directions with higher pressure than that of LSW_2. The propagation Mach number of RSW decreases with an increase in BR because the flow velocity in front of RSW increases. On the other hand, the propagation Mach number of RSW increases with the higher CR because the flow velocity in front of RSW decreases. The propagation Mach number of LSW_3 increases with the higher BR and ER because the pressure behind LSW_3 increases.

The drag coefficient is saturated before REW reaches the pod. The saturated drag coefficient increases with the higher BR because the pressure in front of pod is higher. When REW reaches the pod, the drag coefficient decreases because the pressure across an expansion wave decreases. The rate of decreasing drag coefficient increases with the increase in BR because the minimum drag coefficient is similar regardless of blockage ratio. Therefore, the REW effect with the higher BR is significant.

In this study, the compressible flow phenomena and aerodynamic drag under sudden expansion and contraction of the tube were comprehensively analyzed. The results are expected to benefit the design of Hyperloop system by providing an understanding of the compressible flow effects. Furthermore, this study can aid the design of expanded zones considering the formation of shock wave.

6. Limitations

The idealized shape of the expanded zone was designed in the numerical simulations in order to focus on the general compressible flow phenomena. If the shapes are specified in the future, the analysis can contribute significantly to the development of the Hyperloop system. Additionally, the choked flow between the tube and the pod was assumed in the theoretical consideration. These assumptions are reasonable because the Hyperloop system is designed for transonic speed where the choked flow may occur. The choked flow at the entrance to the expanded zone was also assumed. This assumption limits the range of prediction of normal shock waves, and results in the relative errors between the prediction and simulation. In addition, the fully developed flow and generation of normal shock wave in the expanded zone were assumed. The normal shock wave cannot be generated for a shorter expanded zone. Therefore, the theoretical consideration is applicable for the expanded zone that generates the normal shock wave. Accordingly, the consideration of the choking range and length of the expanded zone in the theoretical prediction can improve the accuracy and generality. Another limitation is that our study analyzed the compressible flow phenomena during the pod movement at the entrance to the expanded zone. More specifically, the analysis of the compressible flow behaviors and aerodynamic characteristics can be useful for designing the sudden expansion and contraction space in the Hyperloop system when the pod moves in the expanded zone. However, our study focused on the compressible flow in the expanded zone when the pod moves in the primary tube. Therefore, the compressible flow phenomena and aerodynamic characteristics in the expanded zone and contraction tube should be analyzed in the future studies.

Declaration of competing interest

The authors declare that they have no known competing financial interests or personal relationships that could have appeared to influence the work reported in this paper.

Acknowledgement

This work was supported by the National Research Foundation of Korea (NRF) grant funded by the Korean government (MEST) [No. 2019R1A2C1087763], the Korea Railroad Research Institute [No. PK2201A1], and the Korea Institute of Energy Technology Evaluation and Planning (KETEP) and the Ministry of Trade, Industry and Energy (MOTIE) of the Republic of Korea [No. 20214000000280].

Appendix A. Supplementary material

Supplementary material related to this article can be found online at https://doi.org/10.1016/j.ast.2022.107587.

References

[1] D. Oster, Evacuated tube transportation, 1999, United State Patent: 5950543.
[2] E. Musk, Hyperloop Alpha, Space X, 2013.
[3] J.S. Oh, T. Kang, S. Ham, K.S. Lee, Y.J. Jang, H.S. Ryou, J. Ryu, Numerical analysis of aerodynamic characteristics of Hyperloop system, Energies 12 (3) (2019) 518.
[4] S. Bibin, S.K. Mukherjea, Numerical investigation of aerodynamic drag on vacuum tube high speed train, in: Proceedings of the ASME 2013 International Mechanical Engineering Congress and Exposition 13, 2013.
[5] H. Kang, Y. Jin, H. Kwon, K. Kim, A study on the aerodynamic drag of transonic vehicle in evacuated tube using computational fluid dynamics, Int. J. Aeronaut. Space Sci. 18 (4) (2017) 614–622.
[6] Y. Zhang, Numerical simulation and analysis of aerodynamic drag on a subsonic train in evacuated tube transportation, J. Mod. Transp. 20 (2012) 44–48.
[7] P. Zhou, J. Zhang, T. Li, Effects of blockage ratio and Mach number on aerodynamic characteristics of the evacuated tube train, Int. J. Rail Transp. 8 (2020) 27–44.
[8] S.A. Gillani, V.P. Panikulam, S. Sadasivan, Z. Yaoping, CFD analysis of aerodynamic drag effects on vacuum tube trains, J. Appl. Fluid Mech. 12 (1) (2019) 303–309.
[9] S. Bao, X. Hu, J. Wang, T. Ma, Y. Rao, Z. Deng, Numerical study on the influence of initial ambient temperature on the aerodynamic heating in the tube train system, Adv. Aerodyn. 2 (2020) 28.
[10] T.T.G. Le, K.S. Jang, K.S. Lee, J. Ryu, Numerical investigation of aerodynamic drag and pressure waves in Hyperloop systems, Mathematics 8 (11) (2020) 1973.
[11] T.K. Kim, K.H. Kim, H.B. Kwon, Aerodynamic characteristics of a tube train, J. Wind Eng. Ind. Aerodyn. 99 (12) (2011) 1187–1196.
[12] J. Niu, Y. Sui, Q. Yu, X. Cao, Y. Yuan, Numerical study on the impact of Mach number on the coupling effect of aerodynamic heating and aerodynamic pressure caused by a tube train, J. Wind Eng. Ind. Aerodyn. 190 (2019) 100–111.
[13] Y. Sui, J. Niu, Y. Yuan, Q. Yu, X. Cao, D. Wu, X. Yang, An aerothermal study of influence of blockage ratio on a supersonic tube train system, J. Therm. Sci. (2020) 1–12.
[14] R. Hruschka, D. Klatt, In-pipe aerodynamic characteristics of a projectile in comparison with free flight for transonic Mach numbers, Shock Waves 29 (2019) 297–306.
[15] K.S. Jang, T.T.G. Le, J. Kim, K.S. Lee, J. Ryu, Effects of compressible flow phenomena on aerodynamic characteristics in Hyperloop system, Aerosp. Sci. Technol. 117 (2021) 106970.
[16] Y. Sui, J. Niu, Q. Yu, Y. Yuan, X. Cao, X. Yang, Numerical analysis of the aerothermodynamic behavior of a Hyperloop in choked flow, Energy 237 (2021) 121427.

[17] D. Tudor, M. Paolone, Optimal design of the propulsion system of a Hyperloop capsule, IEEE Trans. Transp. Electr. 5 (4) (2019) 1406–1418.
[18] J.K. Noland, Prospects and challenges of the Hyperloop transportation system: a systematic technology review, IEEE Access 9 (2021) 28439–28458.
[19] G.H. Trengrouse, M.M. Soliman, Effect of sudden changes in flow area on pressure waves of finite amplitude, J. Mech. Eng. Sci. 8 (2) (1966) 198–206.
[20] W.B. Hall, E.M. Orme, Flow of a compressible fluid through a sudden enlargement in a pipe, Proc. Ins. Mech. Eng. 169 (1) (1955) 1007–1020.
[21] J.D. Anderson, Fundamentals of Aerodynamics, 6th edition, McGraw-Hill, 2016.
[22] J.D. Anderson, Modern Compressible Flow, 3rd edition, McGraw-Hill, 2004.
[23] J. John, T. Keith, Gas Dynamics, 3rd edition, Pearson Education, 2005.
[24] B.A. Maicke, J. Majdalani, R.L. Geisler, Characterization of the startup and pressure blowdown processes in rocket nozzles, Aerosp. Sci. Technol. 25 (1) (2013) 273–282.
[25] B.A. Maicke, G. Bondarev, Quasi-one-dimensional modeling of pressure effects in supersonic nozzles, Aerosp. Sci. Technol. 70 (2017) 161–169.
[26] Y. Huang, H. Xia, X. Chen, Z. Luan, Y. You, Shock dynamics and expansion characteristics of an aerospike nozzle and its interaction with the rotating detonation combustor, Aerosp. Sci. Technol. 117 (2021) 106969.
[27] P.O.A.L. Davies, M.J. Dwyer, A simple theory for pressure pulses in exhaust systems, Proc. Ins. Mech. Eng. 179 (1) (1964) 365–394.
[28] K. Kadoya, N. Matsunaga, A. Nagashima, Viscosity and thermal conductivity of dry air in the gaseous phase, J. Phys. Chem. Ref. Data 14 (4) (1985) 947–970.
[29] F. Menter, Zonal two equation kw turbulence models for aerodynamic flows, in: 23rd Fluid Dynamics, Plasmadynamics, and Lasers Conference, 1993.
[30] Y. Qin, Q. Qu, P. Liu, Y. Tian, Z. Lu, DDES study of the aerodynamic forces and flow physics of a delta wing in static ground effect, Aerosp. Sci. Technol. 43 (2015) 423–436.
[31] N. Jiqiang, S. Yang, Y. Qiujun, C. Xiaoling, Y. Yanping, Y. Xiaofeng, Effect of acceleration and deceleration of a capsule train running at transonic speed on the flow and heat transfer in the tube, Aerosp. Sci. Technol. 105 (2020) 105977.
[32] M.M. Opgenoord, P.C. Caplan, Aerodynamic design of the Hyperloop concept, AIAA J. 56 (11) (2018) 4261–4270.
[33] P. Zhou, J. Zhang, T. Li, W. Zhang, Numerical study on wave phenomena produced by the super high-speed evacuated tube maglev train, J. Wind Eng. Ind. Aerodyn. 190 (2019) 61–70.
[34] J. Braun, J. Sousa, C. Pekardan, Aerodynamic design and analysis of the Hyperloop system, AIAA J. (2017) 4053–4060.
[35] J. Ryu, S.K.L. Sanjiva, K. Viswanathan, Study of supersonic wave components in high-speed turbulent jets using an les database, J. Sound Vib. 333 (25) (2014) 6900–6923.
[36] J. Ryu, K.L. Sanjiva, Instability waves in high-speed jets: near-and far-field DNS/LES data analysis, Int. J. Aeroacoust. 14.3–4 (2015) 643–673.
[37] R.G.M. Hasan, J.J. McGuirk, Assessment of turbulence model performance for transonic flow over an axisymmetric bump, Aeronaut. J. 105 (1043) (2001) 17–32.
[38] C. Fujio, S. Brahmachary, H. Ogawa, Numerical investigation of axisymmetric intake flowfield and performance for scramjet-powered ascent flight, Aerosp. Sci. Technol. 111 (2021) 106531.
[39] G.L.O. Halila, A.P. Antunes, R.G. da Silva, J.L.F. Azevedo, Effects of boundary layer transition on the aerodynamic analysis of high-lift system, Aerosp. Sci. Technol. 90 (2019) 233–245.
[40] R. Prasad, S. Choi, Variable-fidelity aerodynamic analysis of lift fan type aircraft, Aerosp. Sci. Technol. 71 (2017) 636–650.
[41] M. Kandula, R. Nallasamy, P. Schallhorn, L. Duncil, An application of overset grids to payload/fairing three-dimensional internal flow CFD analysis, Eng. Appl. Comput. Fluid Dyn. 2 (1) (2008) 119–129.
[42] Z. Yao, N. Zhang, X. Chen, C. Zhang, H. Xia, X. Li, The effect of moving train on the aerodynamic performances of train-bridge system with a crosswind, Eng. Appl. Comput. Fluid Dyn. 14 (1) (2020) 222–235.
[43] C. Pang, Z. Gao, H. Yang, S. Chen, An efficient grid assembling method in unsteady dynamic motion simulation using overset grid, Aerosp. Sci. Technol. 110 (2021) 106450.
[44] G.L. Halila, J.R. Martins, K.J. Fidkowski, Adjoint-based aerodynamic shape optimization including transition to turbulence effects, Aerosp. Sci. Technol. 107 (2020) 106243.
[45] J.P. Steinbrenner, Automatic structured and unstructured grid cell remediation for overset meshes, in: 52nd Aerospace Sciences Meeting, 2014, p. 0779.
[46] J. Benek, J. Steger, F.C. Dougherty, A flexible grid embedding technique with application to the Euler equations, in: 6th Computational Fluid Dynamic Conference Danvers, 1983, p. 1994.